Modeling and simulation of interstitial fluid flow around an osteocyte in a lacuno-canalicular network

Luoding Zhu (祝罗丁)^{1,*}, Jared Barber¹, Robert Zigon², Sungsoo Na (**나성수**)³,

and Hiroki Yokota (横田博樹)3

- Department of Mathematical Sciences, Indiana University Purdue University Indianapolis, 402 N Blackford Street, LD 270, Indianapolis, IN 46202, USA.
 <u>luozhu@iupui.edu</u>, <u>jarobarb@iupui.edu</u>
- Department of Computer Science, Indiana University Purdue University Indianapolis, , 402 N Blackford Street, Indianapolis, IN 46202, USA.

rzigon@iupui.edu

Department of Biomedical Engineering, Indiana University Purdue University Indianapolis, 723 W Michigan Street, SL 220, Indianapolis, IN 46202

sungna@iupui.edu, hyokota@iupui.edu

* The author to whom correspondence may be addressed: luozhu@iupui.edu

Abstract

Experiments have shown that external mechanical loading plays an important role in bone development and remodeling. In fact, recent research has provided evidence that osteocytes can sense such loading and respond by releasing biochemical signals (mechanotransduction, MT) that initiate bone degradation or growth. Many aspects on MT remain unclear especially at the cellular level. Because of the extreme hardness of the bone matrix and complexity of the microenvironment an osteocyte lives in, in vivo studies are difficult; in contrast, modeling and simulation are viable approaches. Although many computational studies have been carried out, the complex geometry that can involve 60+ irregular canaliculi is often simplified to a select few straight tubes or channels. In addition, the pericellular matrix (PCM) is usually not considered. To better understand the effects of these frequently neglected aspects, we use the lattice Boltzmann equations (LBE) to model fluid flow over an osteocyte in a lacuno-canalicular (LC) network in two dimensions. We focus on the influences of the number/geometry of the canaliculi and the effects of the PCM on the fluid wall shear stress (WSS) and normal stress (WNS) on an osteocyte surface. We consider 16, 32, and 64 canaliculi using one randomly generated geometry for each of the 16 and 32 canaliculi cases and three geometries for the 64 canaliculi case. We also consider 0%, 5%, 10%, 20%, and 40% pericellular matrix density. Numerical results on the WSS and WNS distributions and on the velocity field are visualized, compared, and analyzed. Our major results are: 1) the fluid flow generates significantly greater force on the surface of the osteocyte if the model includes the pericellular matrix (PCM); and 2) in the absence of PCM, the average magnitudes of the stresses on the osteocyte surface are not significantly altered by the number and geometry of the canaliculi despite some quantitative influence of the latter on overall variation and distribution of those stresses; 3) the dimensionless stress (stress after

non-dimensionalization) on the osteocyte surface scales approximately as the reciprocal of the Reynolds number and increasing PCM density in the canaliculi reduces the range of Reynolds number values for which the scaling law holds.

Key words: interstitial flow, viscous incompressible flow, porous media, osteocyte, lacunocanalicular network, mechanotransduction, pericellular matrix, lattice Boltzmann equations, modeling and simulation, wall shear stress, scaling laws

1 INTRODUCTION

As one of the most important human organs, bone serves multiple functions through its complex external and internal structures. Understanding how bone works at all levels is crucial to our health. For example, osteoporosis and bone fracture due to a lack of physical activity (in seniors, the bedridden, and even inactive youth) have become increasingly severe, worldwide healthcare problems [1]. Bone remodeling is due to responses to mechanical signals (e.g., from physical exercise) that regulate critical processes such as bone growth, decay, and healing. Osteocytes [2], which reside in the mineralized bone matrix, play a particularly important role in remodeling as they are responsible for mechanotransduction (MT): the conversion of mechanical stimuli into biochemical signals. In this context MT can lead to either bone formation or degradation.

The main cellular bodies of osteocytes reside in cavities or lacunae that are nested deep within hard calcified bone. A complex network of canaliculi (small canals) radiating outwards from each lacuna connects the encased lacunae to each other. Further connecting the network are osteocyte processes or arms that extend through each of the canaliculi to connect with other osteocyte processes via gap junctions. The osteocytes and their connecting processes are surrounded by a layer of interstitial fluid that separates the cell's membrane from the surrounding bone matrix material (lacuno-canalicular wall). That fluid is filled with cell-associated proteins (pericellular matrix) that can affect flow in the region and resulting stresses on the osteocytes.

Recent studies [3-7] support the following paradigm regarding force-induced bone remodeling. Applying a mechanical stimulus or loading (e.g., walking or running) generates strain on the lacuno-canalicular network (LC; composed of the extracellular matrix that encloses, but does not include, the osteocytes and their surrounding fluid). The strain generates interstitial fluid flow around the osteocytes and through the lacuno-canalicular network and PCM. That pericellular flow exerts forces (e.g., fluid shear stress and normal stress) on the osteocytes. The osteocytes sense (mechanosensation) and respond (mechanoresponse) by converting those mechanical forces into biochemical signals. Those signals can cause osteoclasts to stop degrading bone [8], osteoblasts to form new bone [9], or other bone remodeling activities.

Despite extensive studies, the process by which macroscale forces are eventually sensed is still not fully understood. For instance, studies found that the level of stress that can induce responses in osteocytes *in vitro* is approximately 10 times greater than the typical macroscale stresses experienced by the bone [6, 10]. Somehow the macroscale stress experienced *in vivo* is amplified tenfold at the cellular level by the fluid and osteocyte lacuno-canalicular system (FOLC; includes fluid, osteocytes, and the surrounding extracellular matrix). It is not

completely clear how this stress amplification takes place and which part of the cell actually perceives the amplified mechanical stimuli [1, 4, 7, 8, 11-17]. You et al. [10] and Han et al. [18] developed models showing that elements that tether (tethering elements) the process membrane to the nearby lacuno-canalicular wall and traverse the pericellular space could significantly multiply the strain on the osteocyte process membrane, which offers an explanation for how force amplification could occur. Studies from Weinbaum and Jiang further suggest that the dendritic processes are the primary mechanosensing site [19-21]. At the same time, many other major mechanosensors have also been reported by in vitro and in vivo studies including cytoskeletal components, focal adhesions, intercellular junctions, primary cilia, ion channels, and the extracellular matrix (see a recent review [8] for details). With many mechanosensors identified, there is not yet a clear consensus on exactly how all these potential mechanisms may work together in different scenarios [22]. To help better characterize osteocyte MT, here we consider one potential mechanosensor, the osteocyte cell's main body that lies in the lacuna and is subject to mechanical forces exerted by the interstitial fluid flow in the region.

Because osteocytes live in complex lacuno-canalicular networks encased in hard bone, *in vivo* studies are intractable. Although *in vitro* experiments have been conducted extensively [12, 23-26], they are also limited as they have not yet been able to directly measure desired mechanical forces, such as fluid wall shear stress (WSS) or force distribution on the osteocyte surface. In contrast, mathematical modeling (e.g. [27]) and computational studies have become an indispensable alternative, complementing experiments.

There have been extensive computational studies relevant to the FOLC system in literature. Weinbaum [28] and Klein-Nulend [23] first reported that the fluid flow past an osteocyte process in a narrow canaliculus could produce hydrodynamic stresses of approximately 1.0 Pa. This suggested that the osteocyte processes were responsible for mechanosensing. You et al. [10] and Han et al. [18] speculated the existence of tethering elements and showed such attachments could significantly amplify the stress on the process membrane. Similarly, Yokoyama et al.'s [29] simulations using high-resolution images revealed that tethering elements could cause strain concentration on the process membrane. Kamioka et al. [30] proposed that the inhomogeneous flows induced by the surface roughness of the highly irregular canalicular wall may be an alternative source of stress amplification. Along these lines, Verbbruggen et al. [31] found that the tissue level strain could be significantly amplified if a physiologically realistic computational domain based on real imaging (vs. the simpler domains that are frequently used in other studies, see below) was used. While fluid shear stress (FSS) is believed to be the predominant mechanical stimulus recognized by osteocytes [8, 11, 22], computational results from Anderson et al. [32] suggested that osteocytes are exposed to relatively large fluid wall normal stresses (WNS, i.e., pressure, vs. WSS) in the lacuna in addition to relatively large fluid shear stress in the canaliculi. The potential importance of fluid WNS in the lacuna was later verified by in vitro experiment [33].

Other studies considered larger scale effects of the FOLC system. For instance, Steck and Tate [34] developed a stochastic model for investigating molecular sieving of bone. The model consisted of multiple osteocytes interconnected by a lacuno-canalicular network modelled by randomly distributed cylindrical pores of different diameters. The flow was driven by prescribed pressure gradients, calculated using Darcy's law, and averaged over 20 different random networks. They found that while larger molecules diffuse slower in general, in the networks larger molecules could actually move faster as they are confined to the larger network channels. Their work has implications for the effectiveness of molecules that could either enhance or result from MT.

Due to the complexity of the FOLC system, all mathematical models of the FOLC system have made assumptions and idealizations, including the works previously mentioned. Most models take a coarse-grained approach by representing the 60+ processes/canaliculi with just a few straight tubes or channels. This can fail to capture the effects that a high number of canaliculi may bring to these systems. It can also fail to capture the effects due to the highly irregular geometries that processes and canaliculi can take on in vivo including curving and tapering. For instance, Marsh et al. [35] used molecular dynamic simulations to show that velocity profiles were significantly affected by the shape of a microchannel wall. Anderson and Knothe Tate [36] similarly found that the fluid stresses were significantly underestimated using smooth idealized pericellular geometries vs rougher and more realistic lacuno-canalicular walls. Most works also ignore the PCM because of its complex structure and the lack of laboratory data for its properties. The PCM, however, is relatively densely packed into the salt-water-like fluid that lies between the osteocyte's membrane and the lacunar wall (~ 1 μm thick) and between the process membrane and the canalicular wall (~ 0.3 µm). Fluid mechanics suggests that these omitted components should have some influence on the flows and flow-generated osteocyte forces.

To study how such assumptions may affect study results, we build a two-dimensional model of the FOLC system that incorporates the number and geometry of the canaliculi and the PCM. In our model we consider domains using 16, 32, and 64 canaliculi and randomly chosen geometries that include curved channels. The PCM is modeled using fixed rigid "particles". The "particles" are uniformly and randomly distributed in the lacuna (space between the osteocyte's main body membrane and the lacunar wall) and canaliculi with prescribed density (0, 5, 10, 20, and 40%). The canalicular inlets and outlets are chosen at random because in reality the corresponding boundary conditions are loading and time-dependent and are unknown beforehand. Our focus is on the flow-induced forces on the surface of the osteocyte main body and possible influences of canalicular number/geometry and PCM density on the fluid WSS and WNS and their distributions on the osteocyte body.

The advantage of our modeling framework is its ability to relatively efficiently simulate the complex boundaries of the 60+ canaliculi and model the PCM effect. The modeling framework solves the lattice Boltzmann equations to obtain the fluid flow. An image file in bitmap format generated by Microsoft Paint is utilized to create the complicated flow domain and its boundaries. The novel features of our model include: 1) the canaliculi are modelled as channels of random size and geometry (more physiologically realistic compared to other studies); 2) the PCM is modelled as randomly distributed particles; 3) the canalicular inlets and outlets are chosen at random.

While strong evidence suggests an important role for the process membrane, we only include the osteocyte's main body in this version of the model. This is because it is considered to be one of many potential mechanosensors and is therefore of interest, it is simpler to develop and validate the model without processes (before adding processes in the future), and this version of the model can be used to consider the possible influences of the number and geometry of canaliculi and PCM on flow in the lacuno-canalicular regions. Using this model we can begin to understand the potential effects of these frequently neglected factors and the forces that typically arise on the osteocyte's main body. To the best of our knowledge, such a study has not yet been performed.

The remainder of the paper is organized as follows. Section 2 introduces the mathematical models. Section 3 discusses numerical methods (lattice Boltzmann equations) used for

computer simulation of the models. Section 4 discusses the verification and validation of the numerical methods and their implementations. Section 5 presents the major computational results. Section 6 concludes the article with a summary and discussions.

2. COMPUTATIONAL MODEL

Our computational model in two dimensions of the FOLC system is illustrated in Fig. 1 including 20% PCM. The left panel in Fig.1 shows the model without any PCM. The middle panel shows the model with PCM in the lacuna only; and the right one shows the model with PCM in both the lacuna and the canaliculi. All lacuno-canalicular geometries used in this study are shown in Fig. 2 without any PCM. In lattice Boltzmann (LB) units, the domain $[0.5,1024.5]\times[0.5,1024.5]$ is represented by the model by using lattice points placed on the grid points with coordinates $[1,2,3,...,1024]\times[1,2,3...,1024]$ along the x and y directions, respectively. The osteocyte is idealized as a rigid ellipse (black ellipse centered at $(x_o, y_o) = (512,512)$ with semi-major and semi-minor axes lengths $r_x = 150.4$ and $r_y = 90.855$ in the x and y directions, respectively. The lacuna is situated as another larger concentric ellipse with semi-major and semi-minor axes lengths that are 30 units greater than the osteocyte's (lacuna thickness $l_t = 30$).

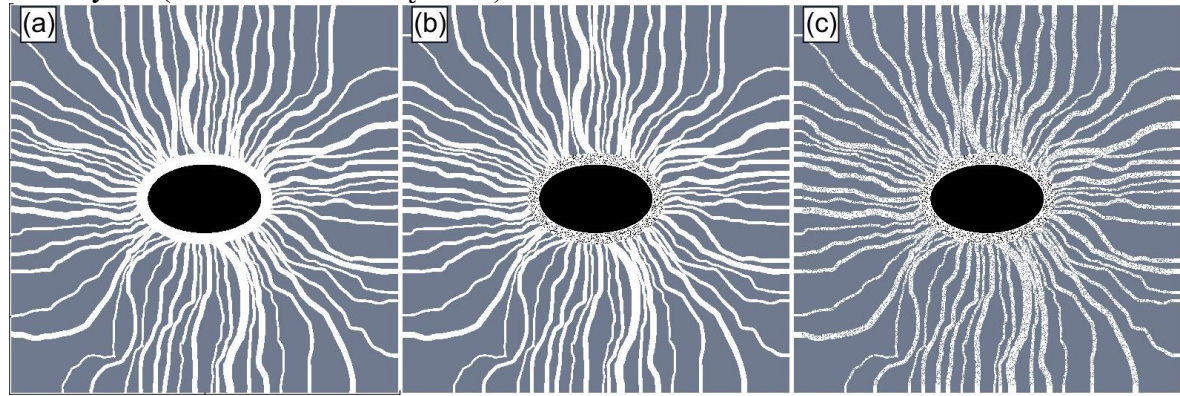


Fig.1. 2D models without PCM (a), with 20% PCM in lacuna (b), and with 20% PCM in both lacuna and canaliculi (c).

The PCM is modelled as many uniformly randomly distributed fixed rigid "particles" (black dots in the lacuna in Fig. 1) in the interstice between the osteocyte surface and lacuna-canalicular outer wall. The particle density ranges between 0% (corresponding to the case when no PCM is considered) and 40% (20% for canaliculi). The particles are chosen as follows. Using a two-dimensional uniform distribution (C++'s rand function), points with coordinates $\mathbf{x} = (x_i, y_j)$ in the original non-PCM fluid computational domain are selected at random as candidates for becoming PCM points. To test if they are in the lacuna region we use the condition that $\frac{(x_i-x_o)^2}{(r_x+l_t)^2} + \frac{(y_j-y_o)^2}{(r_y+l_t)^2} \le 1$. If they are in the lacuna, not in the osteocyte, and are more than 2 units away from the osteocyte boundary (i.e. they are not an (x_f, y_f) or an (x_{ff}, y_{ff}) needed by the Bouzidi boundary conditions addressed below), we change the material at that location from fluid to solid. The algorithm is stopped when the desired PCM density is obtained (to within 0.01%). To encourage better comparisons, any lattice points that are made into PCM in the lower percentage regimes are also made into PCM in the higher percentage regimes.

Some simulations additionally included PCM in the canaliculi regions (right panel in Fig. 1). As done previously, random points were chosen. This time if the particle was outside the lacunar region $\frac{(x_i-x_o)^2}{(r_x+l_t)^2} + \frac{(y_j-y_o)^2}{(r_y+l_t)^2} > 1$, a fluid node, and more than 20 lattice units away

from the outer boundary, the node was changed from fluid to solid. The latter condition simplifies and facilitates code implementation and does not significantly affect our results. The algorithm was stopped when the desired PCM density in the canaliculi region is obtained (to within 0.01%).

The numerous canaliculi of an osteocyte *in vivo* are represented by a number of (64 in Fig. 1 and 16, 32, and 64 in Fig. 2) curved channels (in white) with varying widths and geometries that are chosen randomly. A random canalicular width is chosen for each canaliculus and its corresponding path (geometry) is hand-drawn in MS Paint (details provided below). For the 64 canalicular case, we consider three different geometric configurations that vary in the canalicular widths and directions of travel (geometry) as they head towards the boundaries of the computational domain. The PCM points are the same for all three geometries for a given PCM fraction. Again, to simplify and facilitate the code implementation, the canaliculi are straightened at their intersection with the computational domain for the last 20 lattice points as they head towards the outer boundary. This straightening does not significantly affect any of our results.

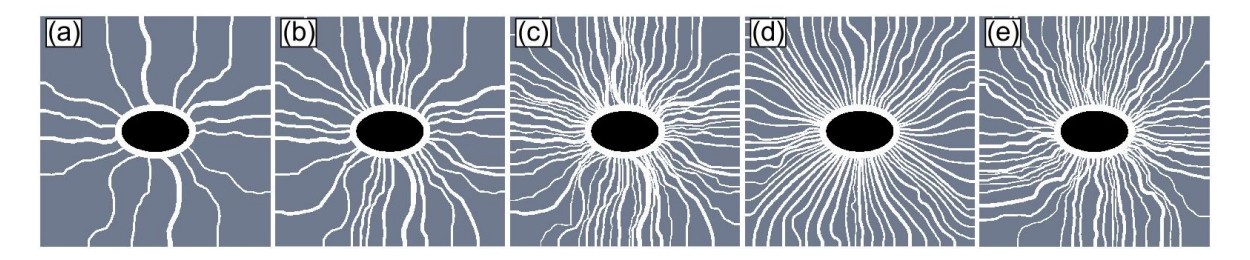


Fig. 2. The 2D geometries used in this study, no PCM included. The (a) and (b) are the 16 and 32 canaliculi cases. For the 64 canaliculi cases we have configurations A (c), B (d), and C (e).

The interstitial fluid filling the lacuna and canaliculi is simplified by representing it with a viscous incompressible fluid (pure water; white in Figs. 1-2). The bone matrix enclosing the FOLC system is modelled as a rigid, stationary solid (gray in Figs. 1-2). Note that cell processes inside the canaliculi are not included explicitly but their effect on flow near the osteocyte is captured to some extent by the PCM "particles" introduced. Inlet and outlet canaliculi are chosen at random (using a coin-flip) to reflect the fact that the flow into or out of a canaliculus depends on the loading process, can vary with time, and is not known beforehand. Fluid velocity is prescribed at the inlets, free outflow conditions are used at the outlets, and a no-slip boundary condition is applied on the surface of the osteocyte, the walls of the lacuna and the canaliculi, and the PCM particles when present (more details below).

The entire white region in Fig. 1 is the flow domain and is relatively complex. Let that domain be denoted by Ω and its boundary by $\partial\Omega$. The partial differential equations governing the motion of a viscous incompressible fluid on Ω are the Navier-Stokes equations:

$$\rho \left(\frac{\partial \mathbf{u}}{\partial t} + \mathbf{u} \cdot \nabla \mathbf{u} \right) = -\nabla \mathbf{p} + \nabla \cdot \mathbf{T} + \mathbf{f}$$

$$\nabla \cdot \mathbf{u} = 0$$
(2)

where **u** is the fluid velocity, p is the pressure, ρ is the mass density, t is the time, and **T** is the deviatoric stress tensor which is defined as $\mathbf{T} = 2\eta \mathbf{D}$, in which **D** is the rate of deformation tensor and η is the fluid dynamic viscosity. Here **f** represents external forces such as gravity which are not considered here ($\mathbf{f} = \mathbf{0}$). Velocity $\mathbf{u} = \mathbf{0}$ is applied on the portions

of the domain boundary $\partial\Omega$ corresponding to the lacuno-canalicular walls. At the inlets the velocity is set to $\mathbf{u}_{in} = (k, 0)$ or $\mathbf{u}_{in} = (0, k)$. The choice for k is discussed below.

3. NUMERICAL METHODS

Although the 2D model appears to be simple, numerically solving the viscous incompressible flow on such a complex domain as in our problem (i.e, finding numerical solutions of Eqs. 1 and 2) is challenging due to the highly complex boundary $\partial\Omega$. A traditional numerical method for solutions of partial differential equations on a complex domain is the finite element method (FEM), which has been frequently used to model bone in the past (see [37-39] for example). A relatively novel alternative, however, is to use the lattice Boltzmann equations (LBE) [40-47] approach. In general, both methods tend to be equally accurate and efficient and both are able to handle complex boundaries. In this particular context, however, the finite element method tends to use an overly fine finite element mesh to resolve the boundary (especially the PCM), which can result in relatively long running solution times. In addition, the LBE has other advantages compared to conventional numerical methods for solving Navier-Stokes equations (including the FEM), because it is relatively easy to implement and parallelize.

Lattice Boltzmann Equations We therefore adopt a lattice Boltzmann model [43, 46], the D2Q9 model, to numerically solve the fluid flow in this complex domain. The D2Q9 model assumes lattice Boltzmann particles reside at each fluid node on a square lattice grid and that they move along nine different directions including a "stationary" direction where they stay motionless at the node. The moving directions of these particles are denoted by ξ_j , j=0,1,2,3,...8 and are given by $\xi_0=(0,0)$, $\xi_1=(1,0)$, $\xi_2=(0,1)$, $\xi_3=(-1,0)$, $\xi_4=(0,-1)$, $\xi_5=(1,1)$, $\xi_6=(-1,1)$, $\xi_7=(-1,-1)$, $\xi_8=(1,-1)$.

For a specific moving direction ξ_j , j = 0,1,2,3,...,8, the distribution function for a single particle velocity, g_j , is evolved via the lattice Boltzmann equation along this direction:

$$g_j(\mathbf{x} + \boldsymbol{\xi}_j, t + 1) = g_j(\mathbf{x}, t) - \frac{1}{\tau} \left(g_j(\mathbf{x}, t) - g_j^0(\mathbf{x}, t) \right) = \tilde{g}_j(\mathbf{x}, t)$$
(3)

where x denotes the spatial position/lattice location, t the time instant, $\tau = \sqrt{3/16} + 0.5$ is the particle relaxation time (see below for more), and g_j^0 the equilibrium distribution function which is given as follows:

$$g_j^0(\mathbf{x},t) = w_j \rho \left(1 + \frac{\boldsymbol{\xi}_j \cdot \mathbf{u}}{c_s^2} + \frac{(\boldsymbol{\xi}_j \cdot \mathbf{u})^2}{2c_s^4} - \frac{\mathbf{u} \cdot \mathbf{u}}{2c_s^2} \right)$$
(4)

where $c_s = c/\sqrt{3}$ (c is the lattice speed defined as the ratio of the lattice spacing $\Delta x = \Delta y$ and time step Δt , which are both set to be 1 in the simulation), and $w_j = 4/9$ for j = 0; $w_j = 1/9$ for j = 1,2,3,4; and $w_j = 1/36$ for j = 5,6,7,8. Note that the right-hand side of Eq (3), denoted by $\tilde{g}_j(\mathbf{x}, t)$, gives what are called the post-collision distribution functions.

Initial Conditions At the initial time, all distribution functions are given by their equilibrium values at all fluid grid nodes where velocity is set as zero $(g_j(\mathbf{x}, 0) = g_j^0(\mathbf{x}, t; \mathbf{u} = \mathbf{0}, \rho = 1))$ except at the inlets $(g_j(\mathbf{x}, 0) = g_j^0(\mathbf{x}, t; \mathbf{u} = \mathbf{u}_{in}, \rho = 1))$ and mass density $(\rho = 1)$ and kinematic viscosity $(\nu = (2\tau - 1)/6)$ are set to be constant. At all later times, the distributions for all fluid nodes are updated using Eq. (3) once per time step until the

simulation termination time. At any given time, the fluid velocities and densities can be recovered using standard lattice Boltzmann formulas involving the particle distributions:

$$\rho = \sum_{j=0}^{8} g_j, \quad \rho \mathbf{u} = \sum_{j=0}^{8} g_j \xi_j.$$

While density can vary in the LBE method, when using the LBE method to describe incompressible flow, the density remains approximately constant. For instance, in our simulations involving incompressible flow, $\rho = 1 \pm 0.1\%$.

Boundary Representations For a complex boundary that includes curved canaliculi walls, as in Fig. 1 and 2, we need a convenient way to generate and describe random geometries. While there are different approaches, here we use Microsoft Paint because it provides a number of tools in its palette for bitmap/domain generation. To generate a given configuration/geometry, we set the canvas size in MS Paint to 1024 × 1024, which corresponds to the desired grid size in LB units for our computational domain. When constructing the original geometry, we use white pixels to denote fluid nodes while black pixels denote solid nodes (osteocyte or bone matrix). (In Figs. 1 and 2, we have introduced gray nodes to more easily delineate osteocyte (black) vs bone matrix (gray) material, but all solid nodes are black during our mesh generation procedures.) To generate a simple shape like the osteocyte ellipse, we use the ellipse and fill tool to generate the ellipse and fill its interior with black pixels. The canaliculi are generated using the paintbrush tool whose size can be specified to create thinner or thicker canaliculi. An additional advantage of this approach is that if a more complex boundary is desired, one can use the zoom feature in MS Paint to magnify and work on the region of interest. After describing the domain, the image is saved as a 1024×1024 bitmap (BMP format). When the simulator is launched, the image file is read using EasyBMP (v. 1.06, Macklin, EasyBMP, http://easybmp.sourceforge.net) and the corresponding lattice Boltzmann mesh generated.

Boundary Conditions The no-slip boundary condition on the rigid lacuno-canalicular walls and the PCM-fluid boundaries is modelled by the half-way bounce-back scheme, which conserves mass at those boundaries. For this boundary condition, when a lattice Boltzmann particle at a fluid node moving along a specific direction hits a rigid wall, it reverses its direction and moves back to the node it originally came from. The corresponding distribution function along that direction at the original node is updated accordingly. When we applied half-way bounce-back boundary conditions to the osteocyte surface (inner boundary of the lacuna), our estimated osteocyte WSS (see estimation procedures below) experienced numerical fluctuations on the order of 50% of the average magnitude of the WSS. Using linear Bouzidi boundary conditions [48], however, changed the variations in our estimates to less than approximately 5% (see Fig. 3).

To understand linear Bouzidi boundary conditions, consider two neighboring nodes in the Lattice-Boltzmann mesh that lie on opposite sides of a curved solid boundary, a fluid node, $x_f = (x_f, y_f)$ and a solid node, $x_s = (x_s, y_s)$. Assume also that the line segment connecting the two nodes (which is parallel to x = constant, y = constant, y = x, or y = -x) intersects at a point on the curve, x_b . Define the relative distance from the fluid node to the boundary curve as $q = \frac{|x_b - x_f|}{|x_s - x_f|}$. Denote the direction from node x_f to x_s as α with the opposite direction from x_s to x_f as $\bar{\alpha}$. Let x_{ff} be the node that is "one node further" from the fluid node in the $\bar{\alpha}$ direction, $x_{ff} = x_f - (x_s - x_f)$. Then the "bounced-back" distribution is given by:

$$g_{\overline{\alpha}}(x_f, t+1) = \begin{cases} (1-2q)\tilde{g}_{\alpha}(x_{ff}, t) + 2q\tilde{g}_{\alpha}(x_f, t), & q < 0.5\\ (1-\frac{1}{2q})\tilde{g}_{\overline{\alpha}}(x_f, t) + \frac{1}{2q}\tilde{g}_{\alpha}(x_f, t), & q \ge 0.5 \end{cases}$$

Note that when q=1/2, we get halfway bounce-back boundary conditions. Also notice the closer we are to the boundary, the more we borrow information from x_{ff} while when we are farther, we borrow some information at x_f regarding the $\bar{\alpha}$ direction from the previous time step to use in the next time step.

Inlets and Outlets At inlets and outlets, the Zou-He (nonequilibrium bounce-back) boundary conditions [49] were employed. At the inlet, the incoming velocity magnitude was specified to be $u_{in} = 4.811e-5$ in LB units. This corresponds to a relaxation coefficient $\tau = \sqrt{3/16} + 1/2$, a characteristic length of 30 lattice units (width of the lacuna), and a Reynolds number of 0.01. The choice of τ makes the LBM flow profile in channel flow match up exactly with Poiseuille flow when the wall is assumed to be halfway between lattice nodes [50]. At outlets a small adjustment is applied to the Zou-He boundary conditions (see details below).

At any inlet or outlet, there are three unknown incoming lattice Boltzmann distribution functions to be determined. For inlets, prescribing the velocities gives us two conditions. The third condition is that the nonequilibrium portion of the outgoing distribution corresponding to the direction that is perpendicular to the wall is reflected back at the boundary, $g_{\overline{\alpha}}(x,t+1) - g_{\overline{\alpha}}^0(x,t+1) = \tilde{g}_{\alpha}(x,t) - \tilde{g}_{\alpha}^0(x,t)$ where \tilde{g} corresponds to the distributions after the collision step takes place and $\bar{\alpha}$ corresponds to the lattice Boltzmann direction opposite of α . The inlet velocity is assumed to be perpendicular to the boundary and its magnitude is specified to be u_{in} (see above).

At outlets, we instead prescribe x and y components of the momentum. To estimate and prescribe the momentum at the next time step at the outlet, we use the momentum at the nodes adjacent to the nodes at the boundary (for a left node we set $\rho_{i_{left},j}\vec{u}_{i_{left},j}$ $\rho_{l_{left}+1,j}\vec{u}_{l_{left}+1,j}$). For the third condition, we again ask for reflection of the nonequilibrium portion of the outgoing distribution. Preliminary results showed use of these boundary conditions conserved mass relatively well over smaller time spans (thousands of time steps) but not over larger time spans (hundreds of thousands of time steps). Given some of our simulations with large PCM percentages were taking on the order of hundreds of thousands of time steps to converge, we adjusted our approach. In particular, we added a correction to the prescribed outgoing flux: $\rho_{i_{left},j}\vec{u}_{i_{left},j} = \rho_{i_{left}+1,j}\vec{u}_{i_{left}+1,j} + K(m_{curr} - m_{des})$ where m_{curr} and m_{des} are the current and desired mass in the system, respectively, and K is an adjustable factor that depends on the geometry of the system. If mass is exactly conserved, the correction term is zero. Due to the fact that our original method conserved mass well on smaller time scales, the correction term was relatively small in all simulations. The value of K, however, does depend somewhat on the FOLC system being considered. In most of our simulations K = 10 was used. In Fig. 3 (for LBM and FlexPDE comparison), K=1 was used (K=10 caused numerical instability in this case). In addition to better mass conservation, the change also sped convergence to steady state by at least tenfold in most simulations.

Computing WNS and WSS Mechanical variables of particular interest are the forces exerted by flow on the osteocyte surface, including wall normal stress (WNS) and wall shear stress (WSS). After exploring several available methods for calculating stresses, we found that using finite differences and interpolation on the calculated velocities and pressures produced results most consistent with the finite element results in Fig. 3. In that method,

stress estimates are made during post-processing after lattice Boltzmann simulations finish. Finite differences are used to produce estimates of velocity derivatives along the y = constant

$$u_{x,b,j} = \frac{u_{f,j} - u_{b,j}}{x_f - x_b}, v_{x,b,j} = \frac{v_{f,j} - v_{b,j}}{x_f - x_b}$$

and x = constant

$$u_{y,i,b} = \frac{u_{i,f} - u_{i,b}}{y_f - y_b}$$
, $v_{y,i,b} = \frac{v_{i,f} - v_{i,b}}{y_f - y_b}$

directions. Here, as before, f corresponds to values at a lattice point adjacent to the boundary, b corresponds to values/estimates at the boundary along either the x = constant or y = constant directions, as delineated above.

The above procedure provides estimates for the derivatives at points on the boundary but the set of locations where we know the x derivatives are not the same as the set of locations where we know the y derivatives. We use interpolation with respect to $\theta = \text{atan2}(y - y_0, x - x_0)$, the polar angle along the ellipse, to obtain estimates of both derivatives whenever the lines $x = x_i$, $y = y_j$, $y - y_j = x - x_i$, and $y - y_j = -(x - x_i)$ cross the ellipse boundary (i.e. all points on the boundary, x_b , that lie between two horizontally, vertically, or diagonally adjacent lattice points). We use two-dimensional extrapolation to obtain values of the pressure ($p = \rho/3$) at the same locations on the boundary. This is done by forming a triangularization using the fluid lattice points and using linear functions on triangles near the boundary to extrapolate pressure values to the boundary (Matlab's function scatteredInterpolant). Having obtained estimates of these variables, we then use the standard formula for the stress tensor to obtain estimates for that tensor on the boundary:

$$\sigma = \mu(\nabla \boldsymbol{u} + (\nabla \boldsymbol{u})^T)/2 - (p - p_{osteo})\boldsymbol{I}$$

Here p_{osteo} is an estimate for the pressure inside the osteocyte that tends to balance external pressure pushing in on the osteocyte. Because we are not modeling fluid flow inside the osteocyte, we estimate p_{osteo} by setting it equal to the average external fluid pressure acting on the osteocyte. On the osteocyte surface/membrane, we calculate stress using unit normal vectors that point out of the membrane (vs into) as well as unit tangent vectors that point counterclockwise along the membrane. This means that a positive normal component of the stress vector $(\mathbf{n} \cdot \boldsymbol{\sigma} \cdot \mathbf{n})$, subsequently referred to as "normal stress" or WNS, corresponds to the fluid pulling outward on the membrane (under tension) while a positive tangential component of the stress vector $(\mathbf{t} \cdot \boldsymbol{\sigma} \cdot \mathbf{n})$, subsequently referred to as "tangential stress" or WSS, corresponds to fluid pulling the membrane in a counterclockwise direction.

4. VERIFICATION AND VALIDATION

For the purposes of verification and validation of the numerical methods and their implementations, we consider a simpler situation: flow past an osteocyte with 4 straight canaliculi (one on each of the 4 sides of the computational domain, Fig. 3). Fluid flows into the domain through the north and south canaliculi and out of the domain using the east and west canaliculi. The problem is numerically solved by our code implementing the lattice Boltzmann methods and by a commercial software FlexPDE [51]. We should note that the finite element mesh uses curved finite elements to resolve the mesh at the corner to within approximately 0.01 lattice Boltzmann units of accuracy while the LBE mesh effectively rounds such intersections to the nearest integer or half integer depending on the feature. To make the finite element mesh align better with the LBE mesh, we smoothed the corners where the lacuna and outlet canaliculi (east and west) intersect using arcs with an approximately 1 pixel radius. The results (flow and force fields) can be seen in Fig. 3.

Panel A) plots the flow speed in the lacuna and canaliculi from the LB method. The units on the x and y axes are lattice Boltzmann length units. The color represents the speed in lattice Boltzmann units (the color bar is on the right hand side). Panel B) plots the relative speed difference between LB methods and FlexPDE in the lacuna region as measured by (LB method speed – FlexPDE speed)/(maximum speed by FlexPDE). The largest differences (<7%) can be seen near the corners where the flow enters and exits the lacuna region. Near the osteocyte, however, differences are < 1%. This is our region of interest. Panel C) plots the normal stress on the wall of the osteocyte as predicted by the LBM (blue) and FlexPDE (red). Panel D) plots the shear stress on the wall of the osteocyte as predicted by LBM (blue) and FPDE (red). In both figures θ represents the angle, in radians, between the positive direction of the x-axis and the line segment connecting a point on the ellipse to the center of the ellipse, measured from the x-axis. The angle is positive if counter-clockwise and negative if clockwise. $\theta = 0$ corresponds to the center of the eastern canaliculus and $\theta =$ $\pm \pi$ corresponds to the center of the western canaliculus. The y-axis represents the normal or shear stress in lattice Boltzmann units, as labeled. One can see that the LBM and FlexPDE methods agree with each other reasonably well.

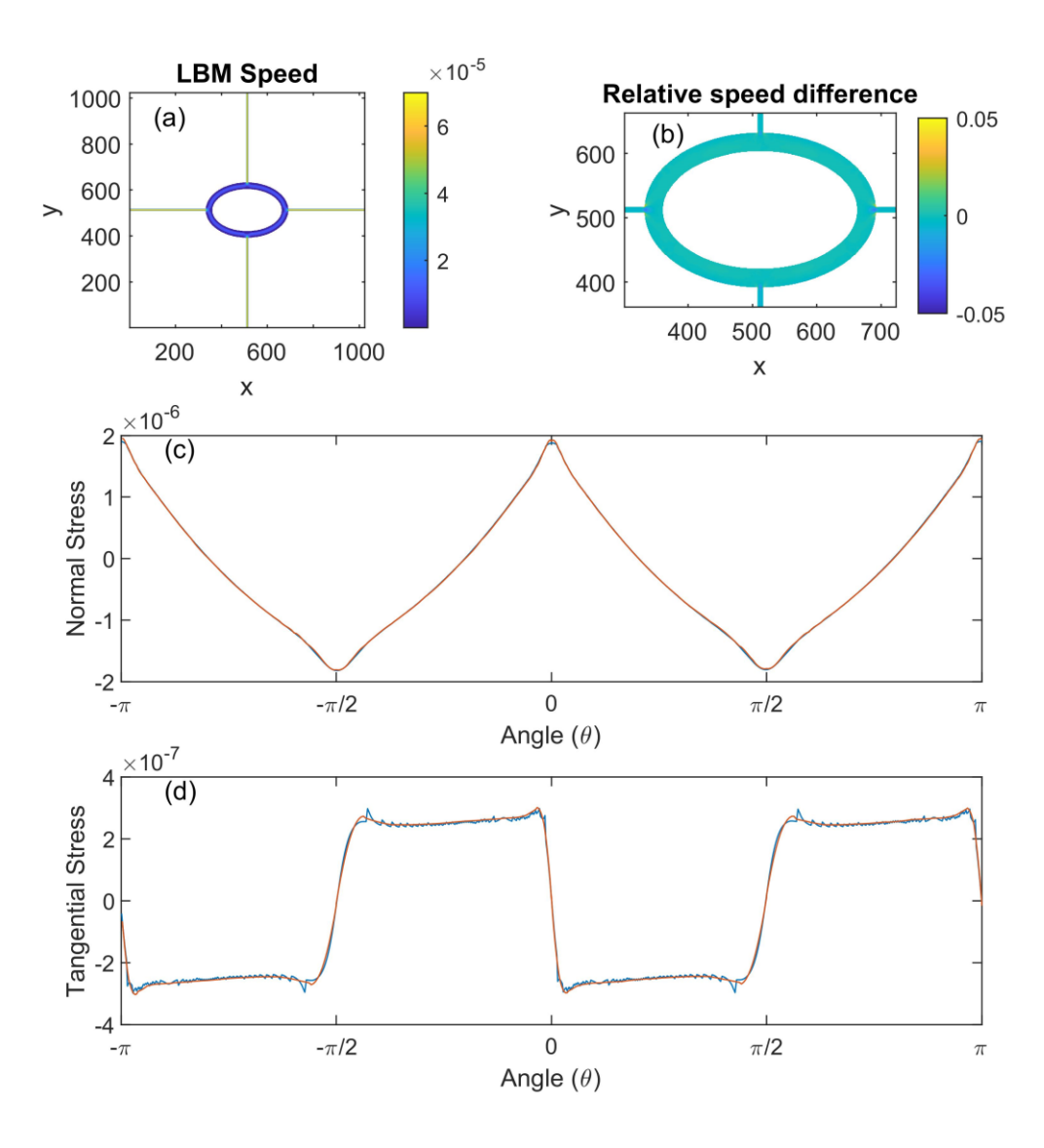


Fig. 3: Comparison of our results and results from the commercial software FlexPDE. (a) Flow speed (in LB units) in the lacuna and canaliculi. (b) Relative speed difference (in percentage) in the region between the two methods. The largest differences, < 7%, can be seen at the corners where the flow enters and exits the lacuna region. Near the osteocyte,

differences are < 1%. (c) Normal and (d) shear stress (in LB units) on the wall of the osteocyte as predicted by LBM (blue) and FlexPDE (red). In both figures θ represents the angle, in radians, between the positive direction of the x-axis and the line segment connecting a point on the ellipse to the center of the ellipse, measured from the x-axis. The angle is positive if counter-clockwise and negative if clockwise. The angle θ has the same meaning in all the subsequent figures. The figure serves as verification and validation of our computational results by the commercial software FlexPDE.

The stress on the osteocyte membranes is difficult to measure directly *in vivo* and *in vitro* due to the complexity of the flow-osteocyte-lacuno-canalicular network. Instead, they are evaluated by theoretical or computational studies (sometimes in conjuction with laboratory experiments). This results in a wide range of stress level estimates (0.01-100 Pa) [6, 11, 32, 37, 39, 52-56]). There is additional uncertainty in these systems as the typical lacuna width can vary from 0.5-8 μ m [57, 58] which may change over time/age [59, 60] and the canalicular flow speed can vary between 0.02 and 1000 μ m/s [11, 30, 32, 39, 53, 55, 57, 61, 62]. Due to this high level of variability, we present our results here (in particular force and stress) in dimensionless form. Given any specific values of the parameters, our results given below can be converted to their dimensional counterparts in SI units. At the same time, we note that using typical literature values for the lacuna width (1 μ m), canalicular flow speed (100 μ m/s), and fluid mass density (10³ kg m³) as well as 10% PCM produces stress estimates in SI units (O(3 Pa)) that lie in the 0.01-100 Pa range.

5. MAJOR COMPUTATIONAL RESULTS

An osteocyte *in vivo* may possess 60+ canaliculi with complex geometries and be surrounded by the PCM. The lattice Boltzmann method has not yet been used with such complex osteocyte-based geometries and low Reynolds number flow. In the first part of our results, we discuss the method's rate of convergence to steady state and how results depend on the Reynolds number. In general, the canaliculi are difficult to incorporate into a computational model because the highly complex geometry can vary greatly. In our model, we consider them by using three different canaliculi numbers, 16, 32, and 64, by using curved channels of variable width, and by using randomly chosen inlets/outlets. These results are presented in the second part of our results section below. Similarly, the effects of the PCM near the osteocyte are not regularly explored due to the complexity of these proteins. Here, we consider the proteins by using the approach previously mentioned and five different PCM percentages in lacuna: 0%, 5%, 10%, 20%, and 40% (the first four in canaliculi). This is presented in the third part of our results below.

The annulus representing the lacuna that surrounds the osteocyte is 30 fluid grid nodes thick in the radial direction. The canaliculi vary in size typically occupying 5 to 15 fluid grid nodes in width. Flow and force fields, in particular, the wall shear and normal forces (WSS and WNS, or tangent and normal forces) applied by the flow on the osteocyte surface, are computed, nondimensionalized, visualized, and compared. Stresses and forces are nondimensionalized by dividing the quantities in LB units by $\rho_{char}u_{char}^2$ and $\rho_{char}u_{char}^2L_{char}$, respectively. Here $\rho_{char}=1$, $u_{char}=u_{in}$, the inlet velocity, and the characteristic length $L_{char}=30$, the width of the lacuna region in LB units. Besides the stresses and forces in this section, all other quantities are in LB units.

A drawback of using lattice Boltzmann methods for low Reynolds number flows is the slow convergence of the solution to its steady state. Typically, the lower the Reynolds number is, the slower the convergence. To make sure solutions are convergent before simulations are terminated, we compare the stesses on the osteocyte surface at every 100,000

steps up to 1M steps for 0% (Fig. 4; starting at 100k) and 20% (Fig. 5; starting at 400k) PCM for $Re = 10^{-6}$. Curves start from light gray (100k) and move towards darker gray and eventually black (1M). The top rows in the figures show the dimensionless stresses along the x-axis, y-axis, normal, and tangential directions on the osteocyte surface, from left to right. The curves in the top rows overlap and no differences can be seen by eye. In the lower rows, the relative difference is defined as ((stress(t = 100 k)-stress($t = t_{later}$))/mean(|stress(t = 100 k)|)) for Fig. 4 and ((stress(t = 400 k)-stress($t = t_{later}$))/mean(|stress(t = 400 k)|)) and are less than about 0.04% in Fig. 4 and 0.03% in Fig. 5 showing little shift in stresses as more time steps are taken. In both cases, waiting 1M LB time steps should be sufficient to assess the stresses at or near steady state.

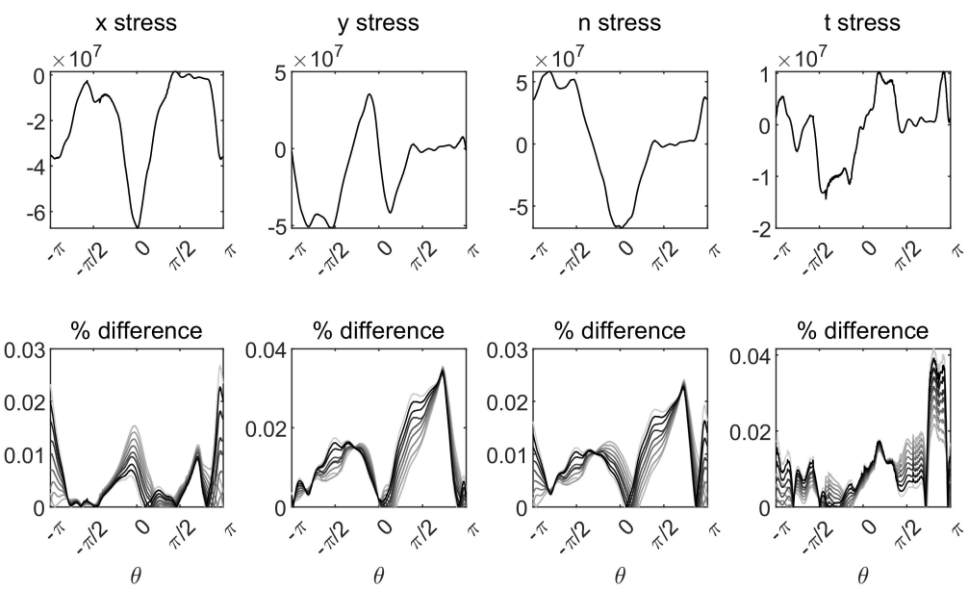


Fig. 4 Stress (dimensionless) at different time steps (first row) and relative differences in percentage (second row). Columns from left to right correspond to stresses along x-axis, y-axis, normal, and tangential directions on osteocyte surface, respectively. The figure shows the convergence of stress in time for models without PCM. $Re = 10^{-6}$.

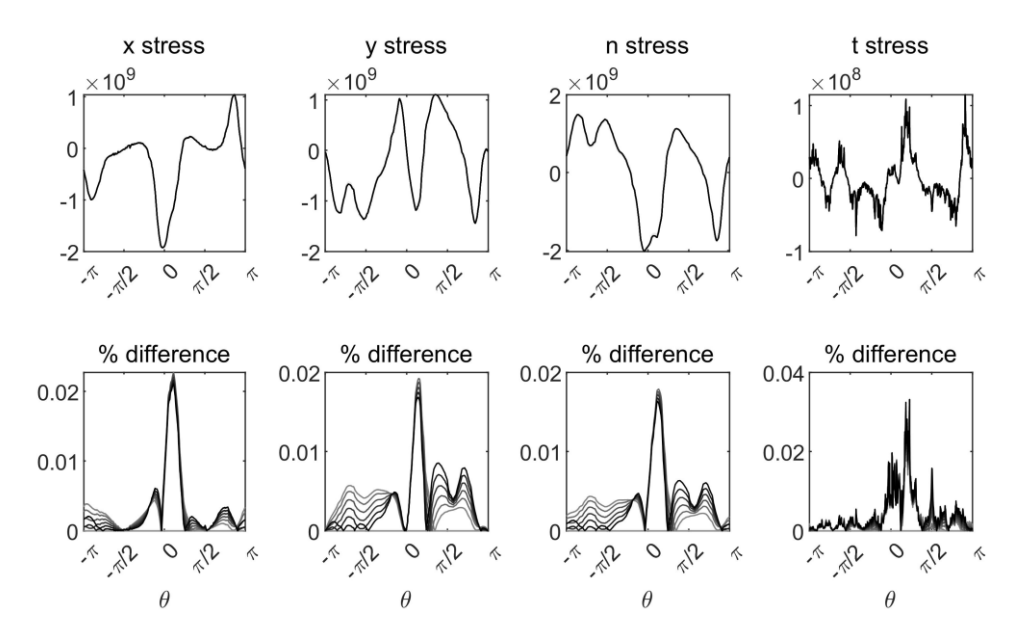


Fig. 5 Stress (dimensionless) at different time steps (first row) and relative differences in percentage (second row) for the case with 20% PCM at time steps 400K, 500K,..., 1M. Columns from left to right correspond to stresses along x-axis, y-axis, normal, and tangential directions on osteocyte surface, respectively. The figure shows the convergence of stress in time for models with PCM. $Re = 10^{-6}$.

To get the small differences in Fig. 5's bottom row, which exhibit similar convergence behavior to those in Fig. 4, we had to wait until t = 400k before performing comparisons. This suggests increasing the PCM density increases the time required to reach steady state, by fourfold in this case when PCM goes from 0 to 20%. Based on this trend and other results, using 100,000 LB time steps is sufficient to assess the stresses at or near steady state when dealing with low PCM densities as in Figs. 6 - 9 while 1M is sufficient for the high PCM densities shown in the other following figures and plots.

Scaling laws are abundant in Nature [63-68]. For flow around an object at small Reynolds number, the drag coefficient scales as the reciprocal of the Reynolds number [69]. The Reynolds number of the interstitial flow in the FOLC system is small and may vary between 10^{-3} to 10^{-9} [30]. It is not immediately clear whether the stress on the osteocyte surface is subject to the same scaling. To investigate the stress scaling, we compute the stresses on the osteocyte surface for 5 different Reynolds numbers (Re= 10^n , n=-2,-3,-4,-5,-6) using 64 canaliculi. We plot the scaled stress (dimensionless stresses multipled by Reynolds number) in Fig. 6: $Re \cdot \Sigma_{\alpha}/\rho u_{in}^2$ where Σ_{α} is the stress along the direction $\alpha = x$, y, normal, or tangential direction. Colors vary from light gray (Re = 0.01) to black ($Re = 10^{-6}$) in top row. Colors vary from light gray (Re = 0.001) to black ($Re = 10^{-6}$) in bottom row. As in Fig. 4-5, it is difficult to discern by eye differences between these scaled stresses (first row). In the second row, we look at the relative difference between the Re = 0.01 case and the other cases, which is defined as ((stress(Re = 0.01)-stress($Re = Re_{lower}$))/mean(|stress(Re = 0.01)|)). This difference is less than 0.3%, which indicates the dimensionless stress indeed scales with the reciprocal of the Reynolds number for $Re \le 0.01$.

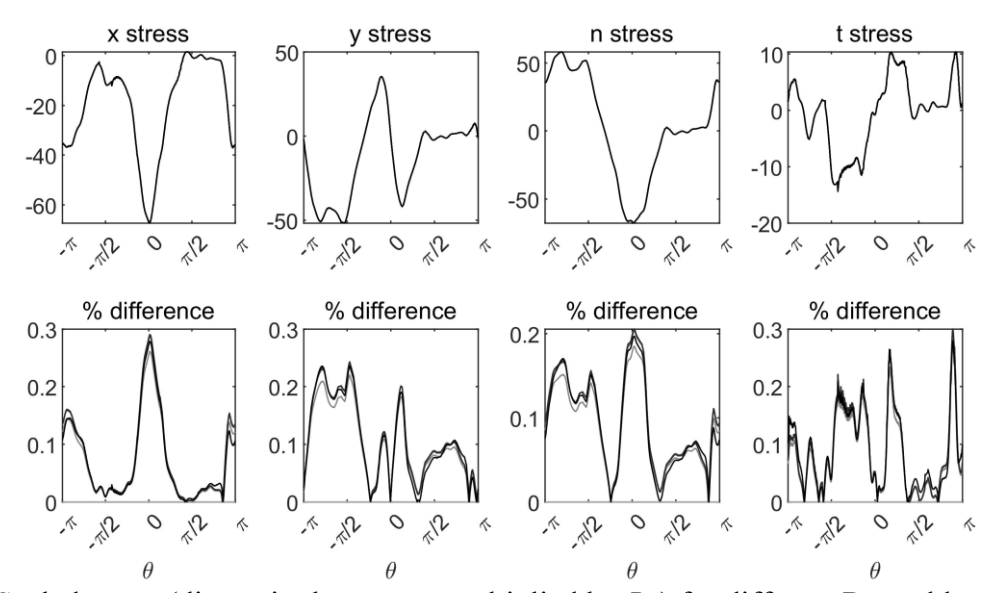


Fig. 6 Scaled stress (dimensionless stress multiplied by Re) for different Reynolds numbers (first row) and relative differences in percentage (second row). Columns from left to right correspond to stresses along the x-axis, y-axis, normal, and tangential directions on the osteocyte surface, respectively. Colors vary from light gray (Re = 0.01) to black ($Re = 10^{-6}$). The figure shows stress scales as 1/Re for $Re \le 0.01$.

We point out that all the simulations for Figs. 4 through 6 use configuration A for 64 canaliculi and the same random set of inlets and outlets. Based on other results (to be discussed below) using hundreds of realizations with different sets of randomly chosen inlets and outlets, we believe the above trends are typical even when inlet and outlet choice is varied. In the remaining account, we use the results with Re = 0.01 as examples.

Fig. 7 plots the WSS and WNS on the osteocyte surface for 16, 32, and 64 canaliculi. In Fig. 7 the geometry and the inlet/outlet of the canaliculi in each case are chosen randomly. The first, second, and third columns plot the cases with 16, 32, and 64 canaliculi, respectively. The first, second, and third rows plot the WNS, WSS, and total force along the x (blue) and y (red) directions on the osteocyte surface, respectively. We see that the quantitative distributions of WNS and WSS on the osteocyte surface do look different for the three cases and the total force even more so (both magnitude and direction). In each case, the total force converges with respect to time quickly. The WNS magnitude is significantly greater than that of the WSS magnitude in each case. This result seems to indicate that the number and geometry of canaliculi do have quantitative influence on the WSS and WNS and their distribution on the osteocyte. Notice that the observed differences may be attributed to a combination of the number, the geometry, and the choice for inlets/outlets of the canaliculi.

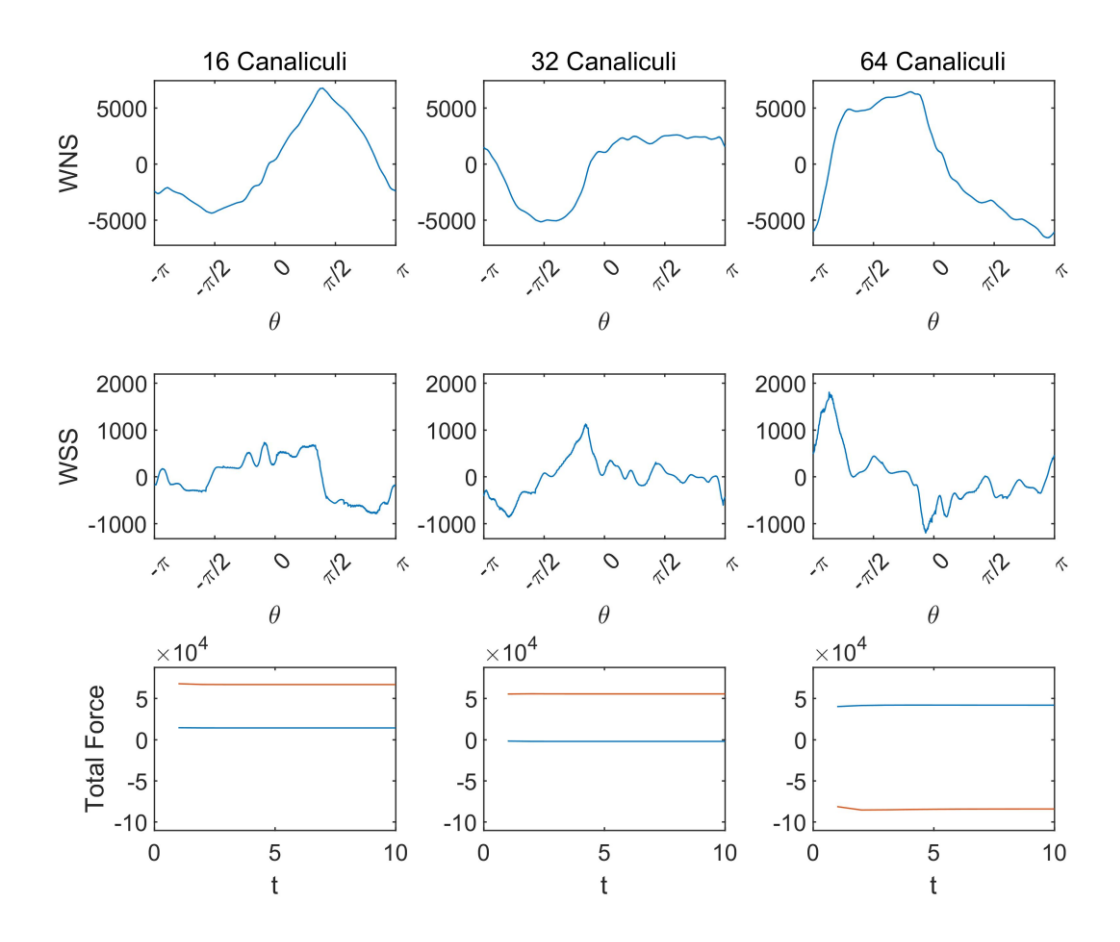


Fig. 7 Dimensionless WNS (first row vs. θ), dimensionless WSS (second row vs. θ), and dimensionless total force (third row vs. t in 10,000s of time steps, 100k time steps total were used) on the osteocyte surface for three cases with 16, 32, and 64 canaliculi (left, middle, and right columns, respectively). The figure shows quantitative differences can

occur when the number and geometry of the canaliculi are varied including WSS and WNS distribution differences.

Fig. 8 plots the WSS and WNS on the osteocyte surface for the case of 64 canaliculi with three different configurations. Note that both the geometry and the inlets/outlets of the canaliculi in each case are chosen randomly. The first, second, and third columns plot the cases with different configurations (the first, second, and third 64 canaliculi cases pictured in Fig. 2), respectively. The first, second, and third rows plot the WNS, WSS, and total force along x (blue) and y (red) directions on the osteocyte surface, respectively. Again one sees that the quantitative distributions of WNS, WSS, and total force on the osteocyte surface are different for the three cases. In each case, the total force converges with respect to time quickly. Also, the magnitude of the WNS is significantly greater than that of the WSS in each case. This seems to indicate that the canaliculi configuration has influence on the WSS and WNS and their distributions on the osteocyte. Notice that the observed differences may be attributed to a combination of the geometry differences and differences in the choice for the inlets/outlets of the canaliculi.

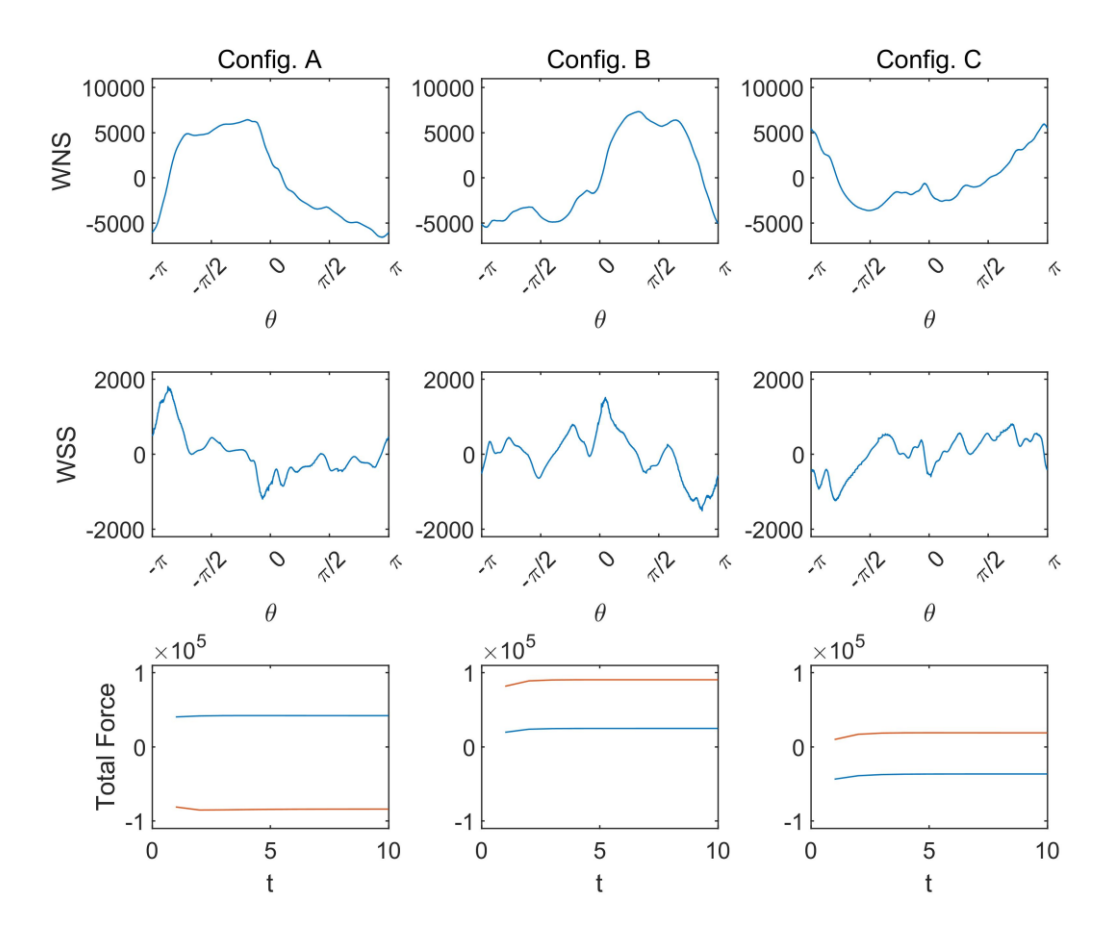


Fig. 8 Dimensionless WNS (first row vs. θ), dimensionless WSS (second row vs. θ), and dimensionless total force on osteocyte surface (third row vs. t in 10,000s of time steps, 100K time steps were used) for the 64 canaliculi cases for three different configurations/geometries (left column A, middle column B, and right column C). The figure shows quantitative differences can occur when the geometry of the canaliculi differ including WSS and WNS distribution differences.

To further understand the above observed potential influences of the number, geometry, and inlets/outlets of the canaliculi on the force field, we perform simulations of 100 realizations

with different randomly chosen inlets and outlets for each of the five cases considered above in Figs. 7 and 8. The mean and standard deviation of the force distributions on the osteocyte surface are computed and plotted in Fig. 9. The first row plots the dimensionless force acting on the osteocyte surface along the x-direction (FX, first column), y-direction (FY, second column), normal direction (WNS, third column)), and the tangential direction (WSS, last column), respectively, for the case with 16 canaliculi. The remaining rows plot the corresponding force distributions for the cases with 32 canaliculi and with 64 canaliculi for each of the three different configurations/geometry. In each panel, the solid red curve corresponds to the mean value as a function of θ and the top and bottom of the shaded region correspond to the standard deviation.

We can see that the quantitative differences in the force distributions (WNS, WSS) among the 5 different cases with 16, 32, and 64 canaliculi are still discernable but they are much less obvious than those in Figs. 7 and 8. This indicates that the major differences observed in Figs 7 and 8 may be attributed to the choice of which canaliculi are inlets and which are outlets. The actual flow inlets and outlets of the canaliculi are in fact unknown *in vivo* and may depend on loading and vary with time (e.g. an inlet at one time may become an outlet at another time, and vice versa). Averaging over 100 realizations of the randomly chosen inlets/outlets may have sufficiently eliminated the inlet/outlet effect. Therefore, it appears that the number and geometry of the canaliculi may not be a major influencing factor with the resulting average force distributions on the osteocyte membrane being *qualitatively* similar regardless of the number and configuration of the canaliculi. This is consistent with a recent work [39]. Given that the number and geometry of an osteocyte's system appear to be relatively random based on *in vivo* studies, this seems to make sense; otherwise, osteocytes would tend towards having some optimal canaliculi number and/or geometry to maximize mechanotransduction effectiveness.

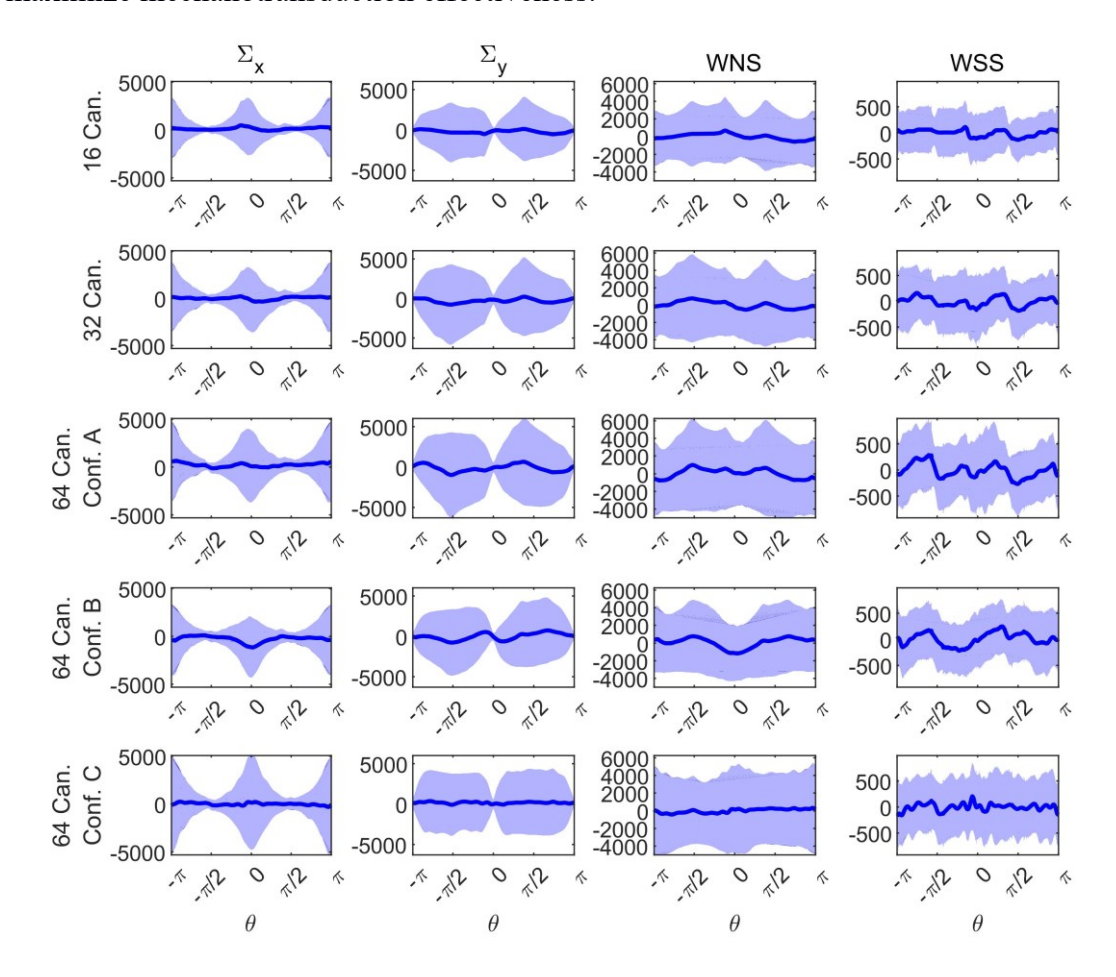


Fig. 9 Mean and standard deviation of 100 realizations for each of the cases considered in Figs 7 and 8. The corresponding dimensionless mean stresses (solid red lines) \pm their standard deviations (top and bottom of the shaded region) are plotted. Rows correspond to the geometries using 16, 32, and 64 (with three configurations A, B, and C) canaliculi, from top to bottom. The columns correspond to the dimensionless force on the membrane acting in the x-direction, y-direction, normal (tension is positive) to the membrane (dimensionless WNS), and tangential (counterclockwise is positive) to the membrane (dimensionless WSS). Relatively little trend can be seen when comparing different numbers of canaliculi and different geometric configurations. The figure shows the number and geometry of canaliculi has less pronounced influence on the WSS and WNS and their distributions on an osteocyte in a lacuna when 100 realizations of simulations with randomly chosen inlets and outlets are averaged.

Now we investigate the possible influence of the PCM. The PCM in vivo is a complex system of fibrous structures and is primarily composed of glycoproteins, proteoglycans, collagens, and fibronectin. To model the PCM in vivo is difficult because of its unknown configuration (geometry and size) and mechanical properties. One approach in 3D is to coarse-grain the PCM and model it as a family of randomly distributed elastic fibers protruding from the lacunocanalicular wall and the cell membrane. An alternative 3D approach is to use Biot's theory modeling the interstitial region as a poroelastic material [70-73]. In principle, these approaches can also be used in 2D. These approaches, however, are challenging in practice because there are 60+ canaliculi each with nontrivial (e.g. curved, tapered, rough-walled) geometry. Here, we instead introduce a different coarse-grained approach. Many rigid immobile particles are randomly introduced in the lacuna and canaliculi to model the PCM. In a 2D simulation, each particle may be regarded as a rigid fiber of infinite length in the third dimension. From the point of view of fluid mechanics, these particles (to first degree) should be able to mimic possible effects of the PCM and tethers on the interstitial flow. The drawback of the 2D part of our approach is that tethers cannot be modelled directly; in 2D tethers would completely block the flow in the canalicular pericellular space.

We consider the addition of PCM in two stages. First we introduce PCM in just the lacuna (middle panel in Fig. 1) and then we add PCM to the canaliculi to consider any additional effects introduced by PCM in that region (right panel in Fig. 1). To verify if the same scaling holds for stress when PCM is introduced in lacuna, we perform simulations with PCM =20% in the lacuna only for $Re=10^n$ where n=-2,-3,-4,-5,-6. Fig. 10 shows similar results as those in Fig. 6. Row 1 shows what the typical stress distributions look like while row 2 shows less than 1.5% relative differences exist for Re < 0.01 (calculated as in Fig. 5 using results at Re = 0.01 as base value). The results suggest the dimensionless stress scales as 1/Re after 20% PCM is introduced in lacuna only.

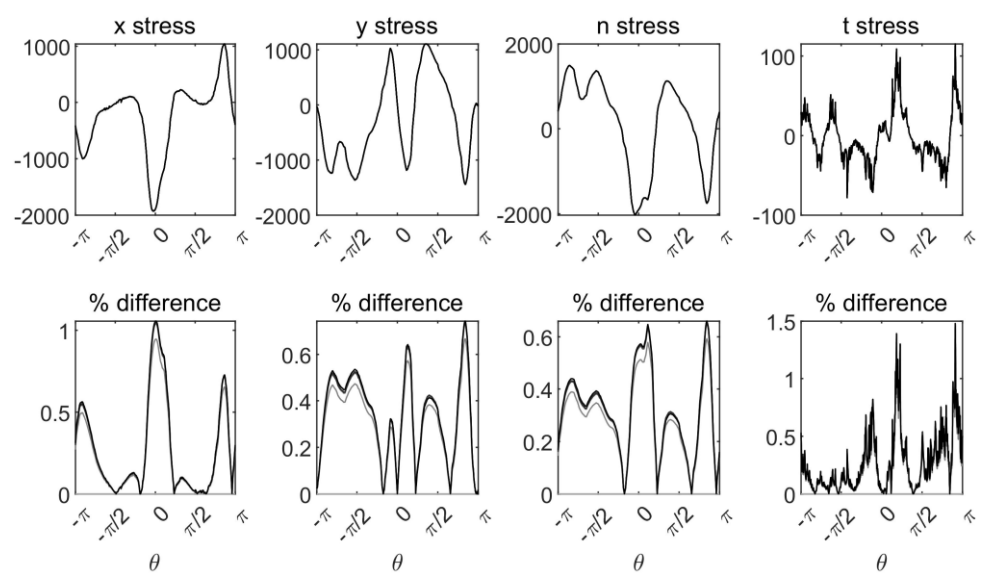


Fig. 10 Scaled stress (dimensionless stress multplied by Re) at different Reynolds numbers (first row) and relative differences in percentage (second row) for the case with 20% PCM in lacuna for Re=10ⁿ, n=-2,-3,-4,-5,-6. Columns from left to right correspond to stresses along x-axis, y-axis, normal, and tangential directions on osteocyte surface, respectively. Colors vary from light gray (Re = 0.01) to black (Re = 10^{-6}). The figure illustrates the stress still scales as 1/Re when 20% PCM is introduced in lacuna for $Re \le 0.01$.

To check if the same scaling holds for stress when PCM is included in both the lacuna and the canaliculi, we perform simulations with PCM = 5% and 20% in both regions for $Re=10^n$, n=-2,-3,-4,-5,-6. Figs. 11 and 12 show similar results as those in Fig. 6 and 10. Row 1 shows what the typical stress distributions look like while row 2 shows approximately 2% and 10% relative differences exist for Re < 0.01 (calculated as in Fig. 6 using results at Re = 0.01 as the base value). Note that the differences among Reynolds numbers among $Re=10^n$, n=-3,-4,-5,-6 are much smaller (0.25% in Fig. 11 and 1.25% in Fig. 12). The results suggest the stress scales approximately as 1/Re for $Re \le 0.01$ when 5% PCM is introduced in both the lacuna and the canaliculi and for $Re \le 0.001$ when PCM with 20% density is introduced in both the lacuna and the canaliculi. Interestingly, it appears that increasing the PCM density in the canaliculi lowers the range of Reynolds numbers for which the stress scaling (1/Re law) holds.

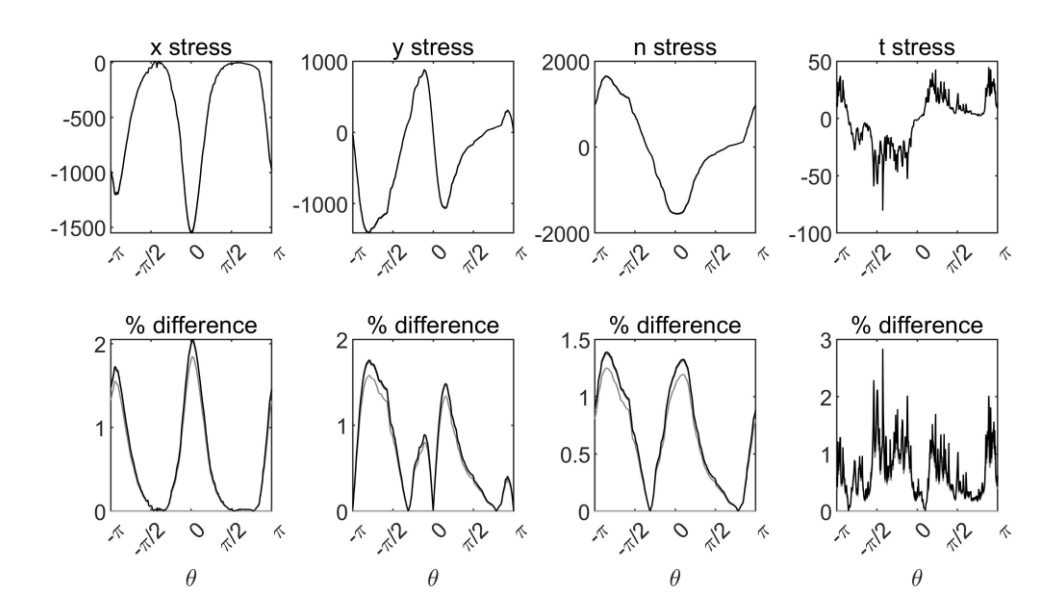


Fig. 11 Scaled stress (dimensionless stress multiplied by Re) at different Reynolds numbers (first row) and relative differences in percentage (second row) for the case with 5% PCM in both the lacuna and the canaliculi for $Re = 10^n$, n=-2,-3,-4,-5,-6. Columns from left to right correspond to stresses along x-axis, y-axis, normal, and tangential directions on the osteocyte surface, respectively. Colors vary from light gray (Re = 0.01) to black ($Re = 10^{-6}$). The figure illustrates the stress approximately scales as 1/Re for $Re \le 0.01$ when PCM with 5% density is introduced in both the lacuna and the canaliculi.

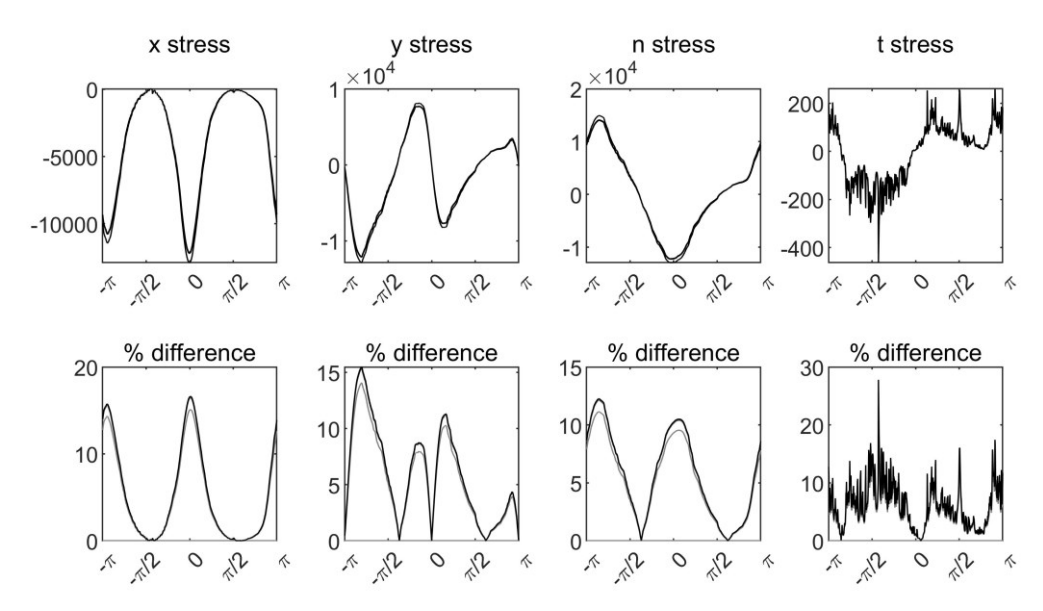


Fig. 12 Scaled stress (dimensionless stress multiplied by Re) at different Reynolds numbers (first row) and relative differences in percentage (second row) for the case with 20% PCM in both the lacuna and the canaliculi for Re= 10^n , n=-2,-3,-4,-5,-6. Columns from left to right correspond to stresses along x-axis, y-axis, normal, and tangential directions on the osteocyte surface, respectively. Colors vary from light gray (Re = 0.01) to black (Re = 10^{-6}). The figure illustrates the stress roughly scales as 1/Re for $Re \le 0.001$ when PCM with 20% density is introduced in both the lacuna and the canaliculi.

Turning to the influence of PCM in the lacuna only on WSS and WNS on the osteocyte, Fig. 13 plots the WNS (the first row), WSS (the second row), and total force (third row) along

the x (blue) and y (red) directions for the case of 64 canaliculi (configuration B, Fig. 3 middle right) with the density varying from 0% (i.e. without PCM, the first column) to 40% (the last column) introduced in lacuna only. The columns from left to right correspond to a density of 0%, 5%, 10%, 20%, and 40%. One can see from the figure that the PCM has a significant influence on the magnitude and distribution of WSS and WNS on the osteocyte: the denser the PCM, the greater the WSS/WNS magnitude and the more oscillation/variation in the distribution. While the rate of convergence of total forces does increase as PCM density increases, all total force trajectories converge relatively quickly with respect to time (last row in Fig. 13). In addition, those trajectories further exhibit significant changes in magnitude as PCM density is increased. We hypothesize the observed difference may be explained by the altered flow path and decreased flow space which causes increased flow speed and velocity gradients and induces greater force magnitude and more variations as the PCM density increases.

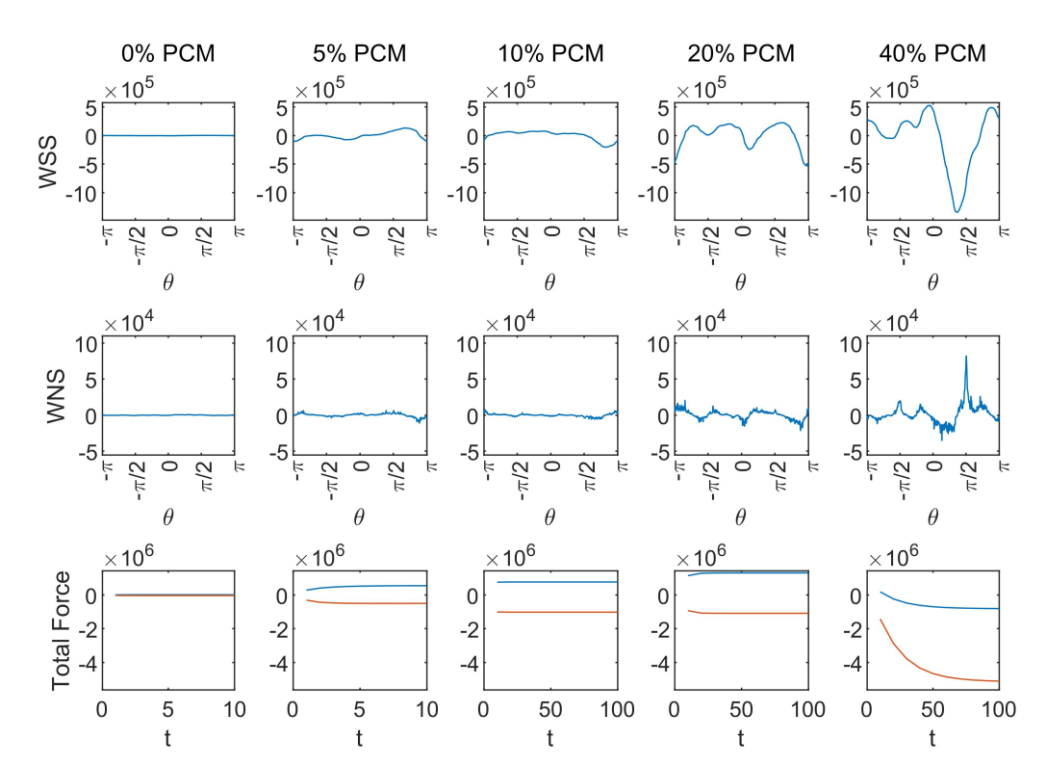


Fig. 13 Dimensionless WSS (first row) and WNS (2^{nd} row) for PCM density of 0%, 5%,10%,20% and 40% (from left to right columns) in lacuna only. The x units for total dimensionless force (last row) corresponds to the number of time steps in ten thousands. The figure shows that increasing the PCM in the lacuna increases the WNS and WSS on the osteocyte body.

Table 1 lists the averaged WNS (top) and WSS (bottom) in magnitude as the PCM density varies from 0 to 40% for the three cases with 16, 32, and 64 canaliculi (averaged over all three configurations). We see that these quantities only vary slightly as the number of canaliculi varies, but they increase significantly as the PCM density increases. Again, this suggests the number/geometry of an osteocyte canalicular structure does not have significant influence on the force acting on the osteocyte membrane but that the PCM density does have significant influence.

Table 1 Average stress magnitude normal to (top) and tangential to (bottom) the osteocyte surface as the PCM density is varied for 16, 32, and 64 canaliculi (16, 32, 64)

Mean(normal	16 Canaliculi	32 Canaliculi	64 Canaliculi
stress)			
0% PCM	3644.1	2664	2709.8
5% PCM	34975	18543	40891
10% PCM	1.13E+05	64157	67257
20% PCM	1.34E+05	6.44E+05	1.14E+05
40% PCM	1.81E+06	2.97E+05	4.08E+05

Mean(shear stress)	16 Canaliculi	32 Canaliculi	64 Canaliculi
0% PCM	423.22	363.84	410.38
5% PCM	875.51	659.27	1131.7
10% PCM	1650	1750.1	1555.7
20% PCM	2982	7716.4	3031.2
40% PCM	16926	7490.2	7508.5

Fig. 14 plots the WNS (the first row), WSS (the second row), and total force (third row) along x (blue) and y (red) directions for the case of 64 canaliculi (configuration B) with the density varying from 0% (i.e. without PCM, the first column) to 20% (the last column) introduced both lacuna and canaliculi. The columns from left to right correspond to a density of 0%, 5%, 10%, 20%. One can see from the figure and a comparison with Fig. 13 that the PCM in canaliculi has a pronounced effect on the magnitude and distribution of WSS and WNS on the osteocyte body in the lacuna. When PCM is placed in the canaliculi, the effective resistance in the canaliculi is significantly raised as it takes much more effort to push fluid through the impeded passage. Before PCM was included in the canaliculi but was included in the lacuna, flow entering the lacuna had the choice of staying in the lacuna or of taking the nearest outflow exit. Due to the relatively low resistance in the no-PCM canaliculi, the nearest outflow exit was taken more frequently than the option of staying in the lacuna. With the PCM in the canaliculi, however, the fluid tending the path of least resistance can no longer "easily" get out the nearest outflow canaliculi; thus causing fluid "crowding" in the lacuna and resulting in greater momentum hence leading to higher forces in general.

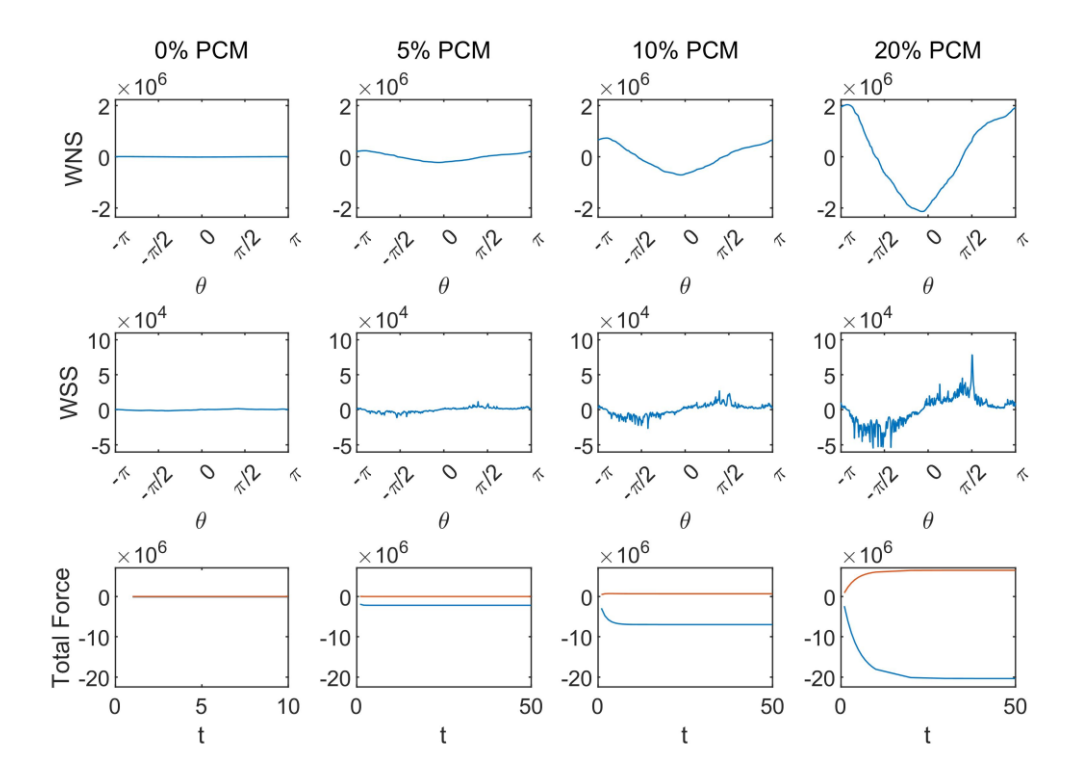


Fig. 14 Dimensionless WNS (frist row) and WSS (2nd row) for PCM in both lacuna and canaliculi with PCM density of 0%, 5%, 10%, 20% (from left to right columns). The units on the horizontal axis in the total dimensionless force plots correspond to the number of time steps in one hundred thousands. Increasing the PCM in both the lacuna and canaliculi increases the WSS and WNS magnitudes and variations similar to the trend in Fig. 13.

Fig. 15 shows the flow field via velocity vectors and speed contours for the case without PCM (top panel), with PCM of density 20% in the lacuna only (middle panel), and in both the lacuna and the canaliculi (bottom panel). In the three panels, the x and y axis coordinates are in LB units. The color bar indicates the flow speed (in LB units) and the arrows denote the velocity directions. We see that the flow in the lacunar region looks more "chaotic" in both the 20% PCM cases compared to the case without PCM. Similarly the flow in the canalicular region looks more "chaotic" in the case of 20% PCM in both the lacuna and the canaliculi (bottom panel) than in the case of 20% PCM in the lacuna only (middle panel). The flow disturbances are caused by the presence of the PCM which deters flow and alters its path. This is consistent with the finding in [74] (PCM blocks flow).

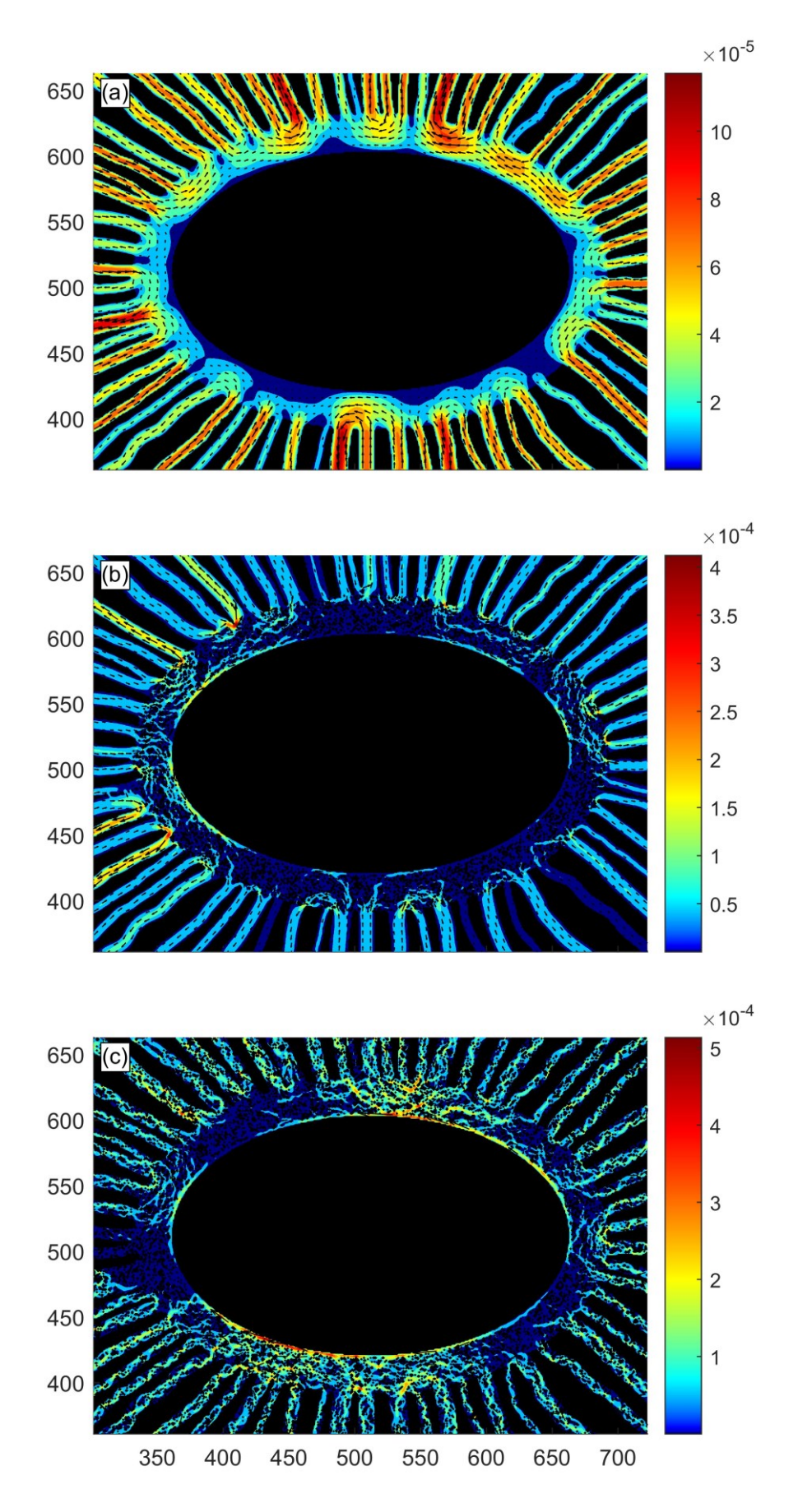


Fig. 15 Flow field of the case without PCM (a), with 20% PCM in the lacuna only (b), and with 20% PCM in both the lacuna and the canaliculi (c). The *x* and *y* axis coordinates are in LB units. The color bar gives the velocity magnitude in LB units. The figure shows the effect of PCM on the flow field. The PCM creates flow disturbances.

We would like to point out that the effect of PCM on flow and force is consistent with previous research [36] which found that the geometry and dimension of the pericellular space within the canaliculi had significant influence on flow and force in the region.

6. SUMMARY AND DISCUSSION

The geometry of the fluid-osteocyte lacuno-canalicular (FOLC) system can be very complex in vivo. In most computational studies, the numerous canaliculi with varying geometries are represented by just a few straight tubes or channels with prescribed inlets/outlets. Similarly, pericellular matrix (PCM) is usually ignored including a failure to fully discuss the possible errors resulting from such omissions. To investigate the possible influences of the number and geometry of the canaliculi and the PCM on the forces generated by the interstitial fluid flow on the cell body in the lacuna, we have introduced a two-dimensional model that can be used to consider the effects of these factors. In the model, the canaliculi are modelled using a varying number of curved randomly shaped channels. The PCM is modelled using fixed rigid "particles" (dots) in the lacuna and canaliculi. The particles are randomly (uniformly) distributed. The inlets and outlets are chosen at random. At inlets velocity is prescibed; at outlets a free outflow condition is used. The complicated interstitial flow in the lacuno-canalicular (LC) network is modelled by the lattice Boltzmann equations (D2Q9 model). The half-way bounce-back scheme is used to model the no-slip boundary condition on the rigid walls of the canaliculi and outer boundary of lacuna; The same boundary condition is used to model the effect of the rigid "particles" that represent the PCM. Linear Bouzidi boundary conditions are used on the osteocyte surface. The Zou-He boundary conditions are used at the inlets and outlets. A series of simulations using a varying number and geometry of canaliculi with and without the PCM being modelled is designed and run with the corresponding computational results visualized and analyzed. Our computational results indicate that 1) Without the PCM, the number and geometry of the canaliculi have some quantitative influence on the WSS and WNS on the osteocyte surface but that the influence on average is not significant; 2) increased PCM density levels produces significant increases in the magnitude of the expected WSS and WNS on the osteocyte's main body; 3) the dimensionless stress on the osteocyte surface scales approximately as the reciprocal of the Reynolds number for $Re \le 0.01$ and the scaling holds for smaller Re when PCM of high density is introduced in both the lacuna and the canaliculi.

The actual physiological boundary conditions are difficult to obtain because the inlets and outlets are loading and time dependent (an inlet may become an outlet and vice versa as time goes by) and the velocity and pressure magnitudes at the inlets/outlets are also time dependent. Because of this uncertainty, we chose to select inlets and outlets at random and use prescribed velocity at inlets and a free outflow condition at outlets. This allows us to consider typical average behavior in such systems.

We also note that in lattice Boltzmann simulations, the actual velocity or pressure magnitudes are less important than the Reynolds number for the system being modeled. In particular, the specific velocity magnitude used in a lattice Boltzmann simulation does not affect the results of a real world problem if the Reynolds number and flow domain geometry remain the same. Further, for small enough Reynolds number (≤ 0.01) we have a scaling law suggesting that the overall typical shapes of the dimensionless WSS and WNS distributions will not change though their magnitudes will scale as 1/Re. Similarly, the lattice Boltzmann pressure can differ by a constant and still provide the same results, as is true for solutions of the Navier-Stokes equations in general. The pressure values used and presented here may not agree with the physiological values (e.g. the Biot theory predicted

fluid pressurization) because of that additive constant. Physiological values, however, may be obtained by comparing the actual value and the computed value at one spatial point. We did not perform the calibration because our focus is not on the flow and force fields of a specific osteocyte in a specific LC network; rather we are interested in how forces change when we change the geometry/number of canaliculi and the PCM of a generic osteocyte in a generic LC network. The latter can be considered without such a calibration.

Biot's theory [70-73] has been used for macroscale modeling and simulation of bone tissue. Applying the theory to an osteocyte in an LC network with PCM at the cellular level would be challenging because of the complicated boundary conditions on the lacuno-canalicular wall of 60+ canaliculi. In our work, a different coarse-grained approach we have decided to use is an alternative approach that has been frequently used by lattice Boltzmann practitioners interested in porous media [46, 75-77], though not in this context. Rigid particles are introduced into lacuna and canaliculi at random to model the PCM. This coarse-gained approach takes into account, to some extent, the effects of PCM, tethers, and even the processes on flow in the pericellular space. While such an approximation is of relatively low accuracy, it can yield insight into the effects that solid material near the osteocyte and in the canaliculi can have on force distributions on the osteocyte's main body.

Additional motivation for our approach that omits explicit modeling of tethers and processes is provided by our desire to keep this initial model parsimonious. Including tethers using this model is not straightforward because in 2D solid material like a tether that connects the canalicular wall and process membrane would block a large portion of flow in the canaliculi. In 3D, flow can go around such obstacles and the flow in 2D would not be mimicking typical 3D flow. Including cellular processes is likewise a task more complicated than the current scope of this work. In vivo, fluid flows around cellular processes that are typically centered in each canaliculus. Centering such processes in the canaliculi and connecting such processes to the osteocyte is particularly difficult when dealing with 60+ canaliculi with nontrivial geometries, as can occur in vivo [78]. Fortunately, the effect of such solid components is partially captured by the particles randomly distributed in the canaliculi. These results suggest that explicitly including processes and tethers would increase force magnitude and variation experienced at the osteocyte's surface and decrease the Reynolds numbers for which the Re scaling law explored here holds. Though we focus here on the osteocyte's main body, our results for PCM in the lacuna also suggest elevated shear stress in the canalicular region in the presence of processes. Schurman et al. [39] suggest higher shear stress tends to be associated with healthier bones. Also, healthy processes tend to widen the canalicular network allowing for better circulation and higher stresses in general. In future work focusing on the processes instead of the osteocyte's main body, we plan to consider processes and tethers more explicitly.

Almost all of the computational studies in literature assume that the interstitial fluid is Newtonian. But the physiologic interstitial fluid may be non-Newtonian [79, 80] since it contains particles such as nutrients, hormones, and other proteins. Additionally, the interstitial flows vary significantly including being oscillatory due to periodic motions such as walking or jogging. In this paper we have investigated the stress on the osteocyte surface under the assumptions that the fluid is pure water (Newtonian) and the flow is steady. We refer readers interested in oscillatory flows of non-Newtonian fluids to the works [81-84] and references therein.

It is well known that the drag coefficient of a rigid body in low Reynolds number flows scales as 1/Re [65, 69] for Re < 1. It is interesting to see that the stress obeys the same

scaling law in our case which is significantly more complicated than flow past an object. This scaling allows one to extrapolate our results that use one Reynolds number to understand what happens at other Reynolds numbers less than 0.01.

The stress and force are given in dimensionless form in the paper; together with the above scaling law, one can convert the dimensionless results in our paper to dimensional counterparts for any given specific configuration of a fluid-osteocyte lanuno-canalicular (FOLC) network. To do this, given the characteristic lacuna width, canalicular flow speed, mass density, and kinematic viscosity of the interstitial fluid, one first calculates the Reynolds number. By the scaling law, one can then obtain the dimensionless force and stress for the Reynolds number in the setting of interest by using the results given in this paper:

 $\Sigma_{\alpha,new} = \frac{Re_{paper}}{Re_{new}} \Sigma_{\alpha,paper} = \frac{0.01}{Re_{new}} \Sigma_{\alpha,paper}$. The corresponding dimensional force and stress in SI units can be obtained by multiplying by $\rho_{new} u_{in,new}^2$, the characteristic mass density times the canalicular flow speed squared.

While agreement in terms of both fluid velocities and stress estimates are good in Fig. 3, some undulations do exist in the lattice Boltzmann stress estimates. Such undulations have also been seen in other studies (e.g. [85]) that more carefully attempt to take the curved boundary into account. The size of such undulations, however, remain small allowing us to make reasonable qualitative observations in our studies. We also note that these undulations are likely due to both the boundary conditions (linear Bouzidi) and the stress estimation procedure implemented here with smoother results likely to result if better boundary conditions and better stress estimation techniques are used.

Lattice Boltzmann methods [45, 86, 87] have been widely used in Computational Fluid Dynamics including flows through porous media [88]. The D2Q9 model used in our work revealed a few drawbacks to using lattice Boltzmann methods for low Reynolds numbers including relatively slow convergence to steady-state solutions and spatial oscillations in shear stress on the osteocyte surface. To overcome these shortcomings, one may use other versions of the lattice Boltzmann methods such as [89] or other approaches mentioned in [90].

The canalicular inlets and outlets of an osteocyte *in vivo* are unknown and may be time and loading dependent. However, in models in the literature, the inlets and outlets are typically prescribed. According to our results, the choice of inlets and outlets may have an influence on the force and flow fields. In our work we take 100 realizations of the randomly selected inlets/outlets to annihilate any possible inlet/outlet effects in our simulations. This allows us to compare results when using different canaliculi number and geometry and see that those factors have relatively little effect. Nonetheless, given 100 realizations, it is somewhat surprising that the mean lines are not flatter than they are. This deserves note as it has to do with inhomogeneity particularly in terms of vessel sizes. Flow in these geometries tends to be dominated by larger vessels which, as estimated by Poiseuille's law, have resistances that are significantly lower than their smaller counterparts (see Fig. 15, top, where larger outlet canaliculi tend to have higher associated speeds within). In two-dimensional Poiseuille flow, resistance is proportional to $1/D^3$ where D is the canaliculi diameter. This can lead to less homogeneous behavior in the system such as the undulations in the mean stresses seen here.

The significantly increased total force (WSS and WNS) on the osteocyte surface seen when the PCM density is increased is probably related to our representation of the PCM using rigid particles in the lacuna and canaliculi. Each particle occupies an effective small region in the shape of a lattice square (otherwise occupied by one fluid node). These particles decrease the effective pericellular space through which the fluid may pass. Since the inflow

velocities are fixed at the inlets in our model, the flow around the osteocyte becomes faster and the velocity gradients become steeper which both induce additional drag force on the osteocyte. Our result is consistent with [31, 74], which leads to a hypothesis that the PCM may amplify the stress on the osteocyte. This phenomenon invites more detailed investigation in the future.

Most research focuses on the stresses on the process membrane in a canaliculus. Here we focus on the stresses on the membrane of the osteocyte's main body. Our stresses, in particular wall shear stress, lie within the range of data in literature. Without any PCM, our stress estimates are in the lower end of the range and smaller than similar estimates made by process models that include no PCM. In that case, the stress on the membrane of the osteocyte's main body is smaller than the stress on the membrane of the processes. Since the lacunar width is considerably wider than the space between the canalicular wall and the process membrane inside a canaliculus and because the flow in the lacuna is less directed that the flow in a canaliculi as it is subject to multiple inlets and outlets entering/exiting the region, it is reasonable to expect that the wall shear stress in the lacuna is typically smaller.

While we have focused here on the stresses on the osteocyte's main body due to studies that have shown it is mechanosensitive [19, 91], it is important to discuss the potential role of the processes, which we have omitted from our study. Multiple computational and experimental studies suggest that osteocyte processes are primarily responsible for mechanosensing [19-21, 23, 28]. Other works, however, have questioned the magnitude of that role. For instance, Yokota et al. [92] reported that the surface area of a process ($\approx 20~\mu m$ long and 50 to 400 nm in diameter) was too small ($< 10 \mu m^2$) for a physiologically realistic 1 Pa shear stress to produce the ≈ 10 pN needed by osteocytes in experiments before they respond. The situation is further complicated by the fact that force sensing macromolecules typically occupy areas far smaller than $10 \mu m^2$. Another study showed that human osteoblasts without processes are mechanosensitive [93]. Similarly, other cultured cell experiments showed that both the osteocyte's main body and its process are mechanosensitive [19, 91]. Some researchers [13, 14] even hypothesised that the osteocyte's body is responsible for mechanical force sensation. Others have identified a potential role for the primary cilium [16, 94] during osteocyte mechanotransduction which, in turn, can be affected by stress on the osteocyte's main body.

With potential roles for the processes, cytoskeletal components, focal adhesions, intercellular junctions, primary cilia, ion channels, and the extracellular matrix [8] and acknowledgement by others that a consensus on MT in osteocytes has not yet been reached [22], we believe an accurate picture of MT requires consideration of these multiple factors. In addition, since many of the potential mechanosensors (e.g. primary cilia and ion channels) are situated on the cell body, in the current work we have focused on the fluid flow force and its distribution along the osteocyte's main body in the lacuna. Our findings here contribute to a better characterization of overall osteocyte MT and, importantly, do not require more explicit modeling of processes for the qualitative results presented here and do not rely on determination of the relative importance of osteocyte's main body vs the processes. We look forward to combining these findings with studies that use processes in the future to help consider such issues.

Our results are obtained from models in two dimensions, in which the cell is modelled as a cylinder of infinite length rather than the actual shape of a physiological osteocyte that has a finite dimension along the third direction. The 3D effect may be significant. Therefore, it is desirable to extend the 2D models to three dimensions to confirm further the findings in

two dimensions. Nevertheless, like the 2D models have done, the 3D models may similarly justify the simplified approach used in existing computational works where the 60+ canaliculi of an osteocyte have been coarse-grained and simplified to be represented by just a few straight tubes.

Like most cells, the osteocyte's main body is deformable under external forcing. Here, it is modelled as a rigid body. Since a deformable body may store elastic potential energy in its body via deformation under external mechanical loading while a rigid body does not, the forces on the surface of the osteocyte may be overestimated to some extent by any rigid model. The same holds true for the modeling of the PCM using rigid rather than flexible proteins.

In the future, we plan to incorporate the cell flexibility in the current model by introducing a fluid-structure-interaction 2D model for the FOLC system, and then extend the model to 3D and incorporate cell deformability there.

ACKNOWLEDGEMENTS

This work was supported by NSF (DMS-1951531, L.Z. and J. B.) and School of Science of IUPUI (the near-miss grant).

Data Availablility Statement

The data that support the findings of this study are available from the corresponding author upon reasonable request.

REFERENCES

- 1. Klein-Nulend, J., R. Bacabac, and A. Bakker, *Mechanical loading and how it affects bone cells: the role of the osteocyte cytoskeleton in maintaining our skeleton.* Eur Cell Mater, 2012. **24**: p. 278-91.
- 2. Tate, M.L.K., J.R. Adamson, A.E. Tami, and T.W. Bauer, *The osteocyte*. The international journal of biochemistry & cell biology, 2004. **36**(1): p. 1-8.
- 3. Nicolella, D.P., D.E. Moravits, A.M. Gale, L.F. Bonewald, and J. Lankford, *Osteocyte lacunae tissue strain in cortical bone*. Journal of biomechanics, 2006. **39**(9): p. 1735-1743.
- 4. Jacobs, C.R., S. Temiyasathit, and A.B. Castillo, *Osteocyte mechanobiology and pericellular mechanics*. Annual review of biomedical engineering, 2010. **12**: p. 369-400.
- 5. Adachi, T., Y. Kameo, and M. Hojo, *Trabecular bone remodelling simulation considering osteocytic response to fluid-induced shear stress.* Philosophical Transactions of the Royal Society of London A: Mathematical, Physical and Engineering Sciences, 2010. **368**(1920): p. 2669-2682.
- 6. Weinbaum, S., Y. Duan, M.M. Thi, and L. You, *An integrative review of mechanotransduction in endothelial, epithelial (renal) and dendritic cells (osteocytes)*. Cellular and molecular bioengineering, 2011. **4**(4): p. 510-537.
- 7. Spyropoulou, A., K. Karamesinis, and E.K. Basdra, *Mechanotransduction* pathways in bone pathobiology. Biochimica et Biophysica Acta (BBA)-Molecular Basis of Disease, 2015. **1852**(9): p. 1700-1708.

- 8. Qin, L., W. Liu, H. Cao, and G. Xiao, *Molecular mechanosensors in osteocytes*. Bone research, 2020. **8**(1): p. 1-24.
- 9. Papachroni, K.K., D.N. Karatzas, K.A. Papavassiliou, E.K. Basdra, and A.G. Papavassiliou, *Mechanotransduction in osteoblast regulation and bone disease*. Trends in molecular medicine, 2009. **15**(5): p. 208-216.
- 10. You, L., S.C. Cowin, M.B. Schaffler, and S. Weinbaum, A model for strain amplification in the actin cytoskeleton of osteocytes due to fluid drag on pericellular matrix. Journal of biomechanics, 2001. **34**(11): p. 1375-1386.
- 11. Rosa, N., R. Simoes, F.D. Magalhães, and A.T. Marques, *From mechanical stimulus to bone formation: a review.* Medical engineering & physics, 2015. **37**(8): p. 719-728.
- 12. Rath, A.L., L.F. Bonewald, J. Ling, J.X. Jiang, M.E. Van Dyke, and D.P. Nicolella, *Correlation of cell strain in single osteocytes with intracellular calcium, but not intracellular nitric oxide, in response to fluid flow.* Journal of biomechanics, 2010. **43**(8): p. 1560-1564.
- 13. Gortazar, A.R., M. Martin-Millan, B. Bravo, L.I. Plotkin, and T. Bellido, *Crosstalk between caveolin-1/extracellular signal-regulated kinase (ERK) and \$\beta\$-catenin survival pathways in osteocyte mechanotransduction*. Journal of Biological Chemistry, 2013. **288**(12): p. 8168-8175.
- 14. Aguirre, J.I., L.I. Plotkin, A.R. Gortazar, M.M. Millan, C.A. O'Brien, S.C. Manolagas, and T. Bellido, *A novel ligand-independent function of the estrogen receptor is essential for osteocyte and osteoblast mechanotransduction*. Journal of Biological Chemistry, 2007. **282**(35): p. 25501-25508.
- 15. Mellon, S. and K. Tanner, *Bone and its adaptation to mechanical loading: a review.* International Materials Reviews, 2012. **57**(5): p. 235-255.
- 16. Temiyasathit, S. and C.R. Jacobs, *Osteocyte primary cilium and its role in bone mechanotransduction*. Annals of the New York Academy of Sciences, 2010. **1192**(1): p. 422-428.
- 17. Isaksson, H., Recent advances in mechanobiological modeling of bone regeneration. Mechanics Research Communications, 2012. **42**: p. 22-31.
- 18. Han, Y., S.C. Cowin, M.B. Schaffler, and S. Weinbaum, *Mechanotransduction and strain amplification in osteocyte cell processes*. Proceedings of the National Academy of Sciences of the United States of America, 2004. **101**(47): p. 16689-16694.
- 19. Burra, S., D.P. Nicolella, W.L. Francis, C.J. Freitas, N.J. Mueschke, K. Poole, and J.X. Jiang, *Dendritic processes of osteocytes are mechanotransducers that induce the opening of hemichannels*. Proceedings of the National Academy of Sciences, 2010. **107**(31): p. 13648-13653.
- 20. Wu, D., M.B. Schaffler, S. Weinbaum, and D.C. Spray, *Matrix-dependent adhesion mediates network responses to physiological stimulation of the osteocyte cell process*. Proceedings of the National Academy of Sciences, 2013. **110**(29): p. 12096-12101.
- 21. Thi, M.M., S.O. Suadicani, M.B. Schaffler, S. Weinbaum, and D.C. Spray, *Mechanosensory responses of osteocytes to physiological forces occur along processes and not cell body and require αVβ3 integrin.* Proceedings of the National Academy of Sciences, 2013. **110**(52): p. 21012-21017.
- 22. Robling, A.G. and L.F. Bonewald, *The osteocyte: new insights*. Annual review of physiology, 2020. **82**: p. 485-506.
- 23. Klein-Nulend, J., A. Van der Plas, C. Semeins, N. Ajubi, J. Frangos, P. Nijweide, and E. Burger, *Sensitivity of osteocytes to biomechanical stress in vitro*. The FASEB Journal, 1995. **9**(5): p. 441-445.
- 24. Kleinnulend, J., C. Semeins, N. Ajubi, P. Nijweide, and E. Burger, *Pulsating fluid flow increases nitric oxide (NO) synthesis by osteocytes but not periosteal*

- fibroblasts-correlation with prostaglandin upregulation. Biochemical and biophysical research communications, 1995. **217**(2): p. 640-648.
- 25. McGarry, J.G., J. Klein-Nulend, M.G. Mullender, and P.J. Prendergast, *A comparison of strain and fluid shear stress in stimulating bone cell responses: a computational and experimental study.* The FASEB journal, 2005. **19**(3): p. 482-484.
- 26. Nauman, E., R. Satcher, T. Keaveny, B. Halloran, and D. Bikle, *Osteoblasts* respond to pulsatile fluid flow with short-term increases in PGE2 but no change in mineralization. Journal of Applied Physiology, 2001. **90**(5): p. 1849-1854.
- 27. Graham, J., B. Ayati, S. Holstein, and J. Martin, *The Role of Osteocytes in Targeted Bone Remodeling: A Mathematical Model.* PLoS ONE, 2013. **8**(5).
- 28. Weinbaum, S., S. Cowin, and Y. Zeng, *A model for the excitation of osteocytes by mechanical loading-induced bone fluid shear stresses*. Journal of biomechanics, 1994. **27**(3): p. 339-360.
- 29. Yokoyama, Y., Y. Kameo, H. Kamioka, and T. Adachi, *High-resolution image-based simulation reveals membrane strain concentration on osteocyte processes caused by tethering elements*. Biomechanics and Modeling in Mechanobiology, 2021. **20**(6): p. 2353-2360.
- 30. Kamioka, H., Y. Kameo, Y. Imai, A.D. Bakker, R.G. Bacabac, N. Yamada, A. Takaoka, T. Yamashiro, T. Adachi, and J. Klein-Nulend, *Microscale fluid flow analysis in a human osteocyte canaliculus using a realistic high-resolution image-based three-dimensional model*. Integrative Biology, 2012. **4**(10): p. 1198-1206.
- 31. Verbruggen, S.W., T.J. Vaughan, and L.M. McNamara, *Strain amplification in bone mechanobiology: a computational investigation of the in vivo mechanics of osteocytes*. Journal of the Royal Society Interface, 2012. **9**(75): p. 2735-2744.
- 32. Anderson, E.J., S. Kaliyamoorthy, J.I.D. Alexander, and M.L.K. Tate, *Nanomicroscale models of periosteocytic flow show differences in stresses imparted to cell body and processes*. Annals of biomedical engineering, 2005. **33**(1): p. 52-62.
- 33. Liu, C., Y. Zhao, W.-Y. Cheung, R. Gandhi, L. Wang, and L. You, *Effects of cyclic hydraulic pressure on osteocytes*. Bone, 2010. **46**(5): p. 1449-1456.
- 34. Steck, R. and M.L.K. Tate, *In silico stochastic network models that emulate the molecular sieving characteristics of bone*. Annals of biomedical engineering, 2005. **33**(1): p. 87-94.
- 35. Marsh, D., S.P. Vanka, I.M. Jasiuk, and M. Knothe Tate. *Molecular dynamics computations of flow in constricted and wavy nano channels.* in *ASME International Mechanical Engineering Congress and Exposition*. 2009.
- 36. Anderson, E.J. and M.L.K. Tate, *Idealization of pericellular fluid space geometry* and dimension results in a profound underprediction of nano-microscale stresses imparted by fluid drag on osteocytes. Journal of biomechanics, 2008. **41**(8): p. 1736-1746.
- 37. Ganesh, T., L.E. Laughrey, M. Niroobakhsh, and N. Lara-Castillo, *Multiscale finite* element modeling of mechanical strains and fluid flow in osteocyte lacunocanalicular system. Bone, 2020. **137**: p. 115328.
- 38. Amirouche, F. and A. Bobko, *Bone remodeling and biomechanical processes-a multiphysics approach*. Austin J Biotechnol Bioeng, 2015. **2**(2): p. 1-11.
- 39. Schurman, C.A., S.W. Verbruggen, and T. Alliston, *Disrupted osteocyte* connectivity and pericellular fluid flow in bone with aging and defective TGF-β signaling. Proceedings of the National Academy of Sciences, 2021. **118**(25).
- 40. Qian, Y.H., *Lattice gas and lattice kinetic theory applied to the Navier-Stokes equations*. Doktorarbeit, Universite Pierre et Marie Curie, Paris, 1990.
- 41. Chen, S. and G.D. Doolen, *Lattice Boltzmann method for fluid flows*. Annual Review of Fluid Mechanics, 1998. **30**: p. 329-364.

- 42. Luo, L.-S., *Unified theory of lattice Boltzmann models for nonideal gases*. Physical review letters, 1998. **81**(8): p. 1618.
- 43. Wolf-Gladrow, D.A., *Lattice-gas cellular automata and lattice Boltzmann models: An Introduction.* 2000: Springer.
- 44. Succi, S., *The Lattice-Boltzmann Equation*. 2001: Oxford university press, Oxford.
- 45. Huang, H., M. Sukop, and X. Lu, *Multiphase lattice Boltzmann methods: Theory and application*. 2015: John Wiley & Sons.
- 46. Guo, Z. and C. Shu, *Lattice Boltzmann method and its applications in engineering*. Vol. 3. 2013: World Scientific.
- 47. Zhu, L., D. Tretheway, L. Petzold, and C. Meinhart, *Simulation of fluid slip at 3D hydrophobic microchannel walls by the lattice Boltzmann method*. Journal of Computational Physics, 2005. **202**(1): p. 181-195.
- 48. Bouzidi, M.h., M. Firdaouss, and P. Lallemand, *Momentum transfer of a Boltzmann-lattice fluid with boundaries*. Physics of fluids, 2001. **13**(11): p. 3452-3459.
- 49. Zou, Q. and X. He, *On pressure and velocity boundary conditions for the lattice Boltzmann BGK model.* Physics of fluids, 1997. **9**(6): p. 1591-1598.
- 50. Krüger, T., H. Kusumaatmaja, A. Kuzmin, O. Shardt, G. Silva, and E.M. Viggen, *The lattice Boltzmann method*. Springer International Publishing, 2017. **10**(978-3): p. 4-15.
- 51. PDE Solutions Inc, *FlexPDE 7: Version 7.17 Documentation*. 2021, Spokane Valley, WA: PDE Solutions Inc.
- 52. Bonewald, L.F. and M.L. Johnson, *Osteocytes, mechanosensing and Wnt signaling*. Bone, 2008. **42**(4): p. 606-615.
- 53. Goulet, G.C., D. Coombe, R.J. Martinuzzi, and R.F. Zernicke, *Poroelastic evaluation of fluid movement through the lacunocanalicular system*. Annals of biomedical engineering, 2009. **37**(7): p. 1390-1402.
- 54. Klein-Nulend, J., A.D. Bakker, R.G. Bacabac, A. Vatsa, and S. Weinbaum, *Mechanosensation and transduction in osteocytes*. Bone, 2013. **54**(2): p. 182-190.
- 55. Verbruggen, S.W., T.J. Vaughan, and L.M. McNamara, *Fluid flow in the osteocyte mechanical environment: a fluid-structure interaction approach*. Biomechanics and modeling in mechanobiology, 2014. **13**(1): p. 85-97.
- 56. Wu, X., N. Wang, Z. Wang, W. Yu, Y. Wang, Y. Guo, and W. Chen, *Mathematically modeling fluid flow and fluid shear stress in the canaliculi of a loaded osteon.*Biomedical engineering online, 2016. **15**(2): p. 261-273.
- 57. Kwon, R.Y. and J.A. Frangos, *Quantification of lacunar–canalicular interstitial* fluid flow through computational modeling of fluorescence recovery after photobleaching. Cellular and molecular bioengineering, 2010. **3**(3): p. 296-306.
- 58. Cardoso, L., S.P. Fritton, G. Gailani, M. Benalla, and S.C. Cowin, *Advances in assessment of bone porosity, permeability and interstitial fluid flow.* Journal of biomechanics, 2013. **46**(2): p. 253-265.
- 59. Coulombe, J.C., Z.K. Mullen, A.M. Wiens, L.E. Fisher, M.E. Lynch, L.S. Stodieck, and V.L. Ferguson, *Reduced local mechanical stimuli in spaceflight diminishes osteocyte lacunar morphometry and spatial heterogeneity in mouse cortical bone.* bioRxiv, 2022.
- 60. Mazur, C. and T. Alliston. Evidence for site-specific mechanoregulation of osteocyte perilacunar/canalicular remodeling. in JOURNAL OF BONE AND MINERAL RESEARCH. 2020. WILEY 111 RIVER ST, HOBOKEN 07030-5774, NJ USA.
- 61. Kwon, R.Y., D.R. Meays, A.S. Meilan, J. Jones, R. Miramontes, N. Kardos, J.-C. Yeh, and J.A. Frangos, *Skeletal adaptation to intramedullary pressure-induced interstitial fluid flow is enhanced in mice subjected to targeted osteocyte ablation*. PLoS One, 2012. **7**(3): p. e33336.

- 62. van Tol, A.F., V. Schemenz, W. Wagermaier, A. Roschger, H. Razi, I. Vitienes, P. Fratzl, B.M. Willie, and R. Weinkamer, *The mechanoresponse of bone is closely related to the osteocyte lacunocanalicular network architecture*. Proceedings of the National Academy of Sciences, 2020. **117**(51): p. 32251-32259.
- 63. Wautelet, M., *Scaling laws in the macro-, micro-and nanoworlds*. European Journal of Physics, 2001. **22**(6): p. 601.
- 64. West, G.B. and J.H. Brown, *Life's universal scaling laws*. Physics today, 2004. **57**(9): p. 36-43.
- 65. Zhu, L., Scaling laws for drag of a compliant body in an incompressible viscous flow. Journal of Fluid Mechanics, 2008. **607**: p. 387-400.
- 66. Liu, K., M. Allahyari, J. Salinas, N. Zgheib, and S. Balachandar, *Investigation of theoretical scaling laws using large eddy simulations for airborne spreading of viral contagion from sneezing and coughing.* Physics of Fluids, 2021. **33**(6): p. 063318.
- 67. Gupta, S., A. Sharma, A. Agrawal, M.C. Thompson, and K. Hourigan, *Hydrodynamics of a fish-like body undulation mechanism: Scaling laws and regimes for vortex wake modes.* Physics of Fluids, 2021. **33**(10): p. 101904.
- 68. Alben, S., M. Shelley, and J. Zhang, *Drag reduction through self-similar bending of a flexible body.*
- 69. Batchelor, C.K. and G. Batchelor, *An introduction to fluid dynamics*. 2000: Cambridge university press.
- 70. Kameo, Y., Y. Ootao, and M. Ishihara, *Poroelastic analysis of interstitial fluid flow in a single lamellar trabecula subjected to cyclic loading*. Biomechanics and modeling in mechanobiology, 2016. **15**(2): p. 361-370.
- 71. Le Pense, S. and Y. Chen, Contribution of fluid in bone extravascular matrix to strain-rate dependent stiffening of bone tissue—A poroelastic study. Journal of the Mechanical Behavior of Biomedical Materials, 2017. **65**: p. 90-101.
- 72. Sun, W., On the theory of Biot-patchy-squirt mechanism for wave propagation in partially saturated double-porosity medium. Physics of Fluids, 2021. **33**(7): p. 076603.
- 73. Biot, M.A., *General theory of three-dimensional consolidation*. Journal of applied physics, 1941. **12**(2): p. 155-164.
- 74. Anderson, E.J., S.M. Kreuzer, O. Small, and M.L.K. Tate, *Pairing computational and scaled physical models to determine permeability as a measure of cellular communication in micro-and nano-scale pericellular spaces*. Microfluidics and nanofluidics, 2008. **4**(3): p. 193-204.
- 75. White, J.A., R.I. Borja, and J.T. Fredrich, *Calculating the effective permeability of sandstone with multiscale lattice Boltzmann/finite element simulations*. Acta Geotechnica, 2006. **1**(4): p. 195-209.
- 76. Boek, E.S. and M. Venturoli, *Lattice-Boltzmann studies of fluid flow in porous media with realistic rock geometries*. Computers & Mathematics with Applications, 2010. **59**(7): p. 2305-2314.
- 77. Kang, Q., *Lattice Boltzmann simulation of flow in porous media*. 2004: The Johns Hopkins University.
- 78. You, L.-D., S. Weinbaum, S.C. Cowin, and M.B. Schaffler, *Ultrastructure of the osteocyte process and its pericellular matrix*. The Anatomical Record Part A: Discoveries in Molecular, Cellular, and Evolutionary Biology, 2004. **278**(2): p. 505-513.
- 79. Lemaire, T., S. Naïli, and A. Rémond, Study of the influence of fibrous pericellular matrix in the cortical interstitial fluid movement with hydroelectrochemical effects. Journal of biomechanical engineering, 2008. **130**(1).

- 80. Kumar, R., A.K. Tiwari, D. Tripathi, and A. Mishra, *Electromagnetic Field Induced Alterations in Fluid Flow through Lacuno-Canalicular System of Bone*. International Journal of Mechanical Sciences, 2021: p. 107036.
- 81. Gilbert, P.H. and A.J. Giacomin, *Molecular origins of higher harmonics in large-amplitude oscillatory shear flow: Shear stress response.* Physics of Fluids, 2016. **28**(10): p. 103101.
- 82. Saengow, C., A.J. Giacomin, and C. Kolitawong, *Exact analytical solution for large-amplitude oscillatory shear flow from Oldroyd 8-constant framework: Shear stress.* Physics of Fluids, 2017. **29**(4): p. 043101.
- 83. Jbara, L.M., A.J. Giacomin, and C. Saengow, *Pattern method for higher harmonics of first normal stress difference from molecular orientation in oscillatory shear flow.* Physics of Fluids, 2020. **32**(3): p. 031704.
- 84. Giacomin, A., L. Jbara, and C. Saengow, *Pattern method for higher harmonics from macromolecular orientation in oscillatory shear flow.* Physics of Fluids, 2020. **32**(1): p. 011703.
- 85. Mei, R., D. Yu, W. Shyy, and L.-S. Luo, *Force evaluation in the lattice Boltzmann method involving curved geometry*. Physical Review E, 2002. **65**(4): p. 041203.
- 86. Petersen, K. and J. Brinkerhoff, On the lattice Boltzmann method and its application to turbulent, multiphase flows of various fluids including cryogens: A review. Physics of Fluids, 2021. **33**(4): p. 041302.
- 87. Succi, S. and S. Succi, *The lattice Boltzmann equation: for complex states of flowing matter*. 2018: Oxford University Press.
- 88. Li, S., F. Jiang, B. Wei, J. Hou, and H. Liu, *Prediction of three-phase relative permeabilities of Berea sandstone using lattice Boltzmann method.* Physics of Fluids, 2021. **33**(6): p. 063302.
- 89. Khirevich, S. and T.W. Patzek, *Behavior of numerical error in pore-scale lattice Boltzmann simulations with simple bounce-back rule: Analysis and highly accurate extrapolation.* Physics of Fluids, 2018. **30**(9): p. 093604.
- 90. Phan, A., D. Fan, and A. Striolo, *Fluid transport through heterogeneous pore matrices: Multiscale simulation approaches.* Physics of Fluids, 2020. **32**(10): p. 101301.
- 91. Goggin, P., K. Zygalakis, R. Oreffo, and P. Schneider, *High-resolution 3D imaging of osteocytes and computational modelling in mechanobiology: insights on bone development, ageing, health and disease.* Eur Cell Mater, 2016. **31**: p. 264-295.
- 92. Yokota, H., A. Tovar, and A. Robling, *Dynamic muscle loading and mechanotransduction*. Bone, 2012. **51**(4): p. 826-827.
- 93. Kapur, S., D.J. Baylink, and K.-H.W. Lau, Fluid flow shear stress stimulates human osteoblast proliferation and differentiation through multiple interacting and competing signal transduction pathways. Bone, 2003. **32**(3): p. 241-251.
- 94. Duffy, M.P., The osteocyte primary cilium is a mechanoresponsive organelle that regulates cytoskeletal adaptation and coordinates mechanotransduction with adenylyl cyclases. 2021, Columbia University.